Geographical distribution and interseasonal variability of tropical deep convection: UARS MLS observations and analyses

Jonathan H. Jiang,[1] Bin Wang,[2] Kenshi Goya,[3] Klemens Hocke,[4] Stephen D. Eckermann,[5] Jun Ma,[6] Dong L. Wu,[1] and William G. Read[1]

Received 8 May 2003; revised 21 November 2003; accepted 2 December 2003; published 13 February 2004.

[1] Tropical deep convection and its dynamical effect on the tropopause and stratosphere are investigated using a suite of data from the Upper Atmospheric Research Satellite (UARS) Microwave Limb Sounder (MLS), including upper tropospheric humidity, cloud radiance, and gravity wave measurements. For this purpose, geographical distributions of temperature, water vapor, and cloudiness in the tropical tropopause layer (TTL) are compared with corresponding maps of gravity wave variance in the stratosphere. In addition, ECMWF global wind divergent and velocity potential fields as well as NOAA outgoing longwave radiation and CMAP rainfall data are analyzed to help pinpoint the locations of deep convection. We found that high-altitude clouds near the bottom of TTL ($\sim$147 hPa) are usually surrounded by high-humidity air, and their spatial pattern and seasonal variability are closely associated with regions of vigorous summertime deep convection. Upward propagating gravity waves generated from these convection regions are shifted poleward by prevailing stratospheric winds. We estimate that tropical deep convection lifts $\sim$5% of the cloud tops to altitudes above 100 hPa and that most of the extreme deep convection events occur in the Western Pacific and Indian monsoon regions. Low-temperature regions in the TTL are associated with, but often drift away from, the center of deep convection. Regions of water vapor maxima near the bottom of TTL are located directly above the deep convection centers, but this moisture behavior is somewhat reversed at the top of the TTL. The integrated picture derived from this study implies that convective scale motions could be important in affecting short-term dehydration processes in the TTL. Our results also suggest that the spatial organization and temporal development of tropical convective systems will be better monitored with the follow-on Earth Observing System (EOS) Aura satellite instruments and lead to improved understanding of the complex interaction of tropical convection with large-scale dynamic and thermodynamic conditions. *INDEX TERMS:* 3314 Meteorology and Atmospheric Dynamics: Convective processes; 3362 Meteorology and Atmospheric Dynamics: Stratosphere/troposphere interactions; 3374 Meteorology and Atmospheric Dynamics: Tropical meteorology; *KEYWORDS:* convective processes, gravity waves, stratosphere-troposphere interaction, tropical meteorology

Citation: Jiang, J. H., B. Wang, K. Goya, K. Hocke, S. D. Eckermann, J. Ma, D. L. Wu, and W. J. Read (2004), Geographical distribution and interseasonal variability of tropical deep convection: UARS MLS observations and analyses, *J. Geophys. Res.*, *109*, D03111, doi:10.1029/2003JD003756.

[1]Jet Propulsion Laboratory, California Institute of Technology, Pasadena, California, USA.
[2]Department of Meteorology, University of Hawaii, Honolulu, Hawaii, USA.
[3]Geophysical Fluid Dynamics Laboratory, Kyushu University, Hakozaki, Fukuoka, Japan.
[4]Max-Planck-Institut fur Aeronomie, Katlenburg-Lindau, Germany.
[5]Middle Atmosphere Dynamics Section, Naval Research Laboratory, Washington, D.C., USA.
[6]Computational Physics Inc., Springfield, Virginia, USA.

0148-0227/04/2003JD003756$09.00

1. Introduction

[2] Convection is formed from convective warming of mid-troposphere initiated by a surface warming [*Holton*, 1992]. Deep convection is a more vertically developed and localized convection event that is characterized by rapid injection of boundary layer air near or through the tropopause. Cloud or cloud systems formed by condensation in these convecting air masses near the tropics are the primary mechanism by which solar heat moves from the ocean upward into the free troposphere, where it can be transported poleward and eventually emitted to space. In the process, these great engines of the global climate produce precipitation and drive the global-scale circula-

tion. The combined effect of these convective systems and the large-scale circulation with which they interact determines the cloudiness, moisture, and temperature structure of tropical troposphere, which in turn plays a central role in determining the global climate.

1.1. Water Vapor Transport Across the Tropical Tropopause

[3] Tropical deep convection is also the main source of upper-tropospheric humidity (UTH), which plays an important role in maintaining the natural greenhouse effect in the atmosphere. The maximum level of neutral buoyancy near the tropics is around 14 km (~150 hPa) [*Highwood and Hoskins*, 1998], which is the level of convective equilibrium of the tropical troposphere. Rapid ascending air masses generated by deep convection can overshoot this convective equilibrium level and reach as high as ~18 km (~70 hPa) [*Sherwood and Dessler*, 2000], which is near the level of radiative equilibrium of the stratosphere (i.e., the lowermost stratosphere). The region between the tropospheric convective equilibrium and the stratospheric radiative equilibrium around the tropics is referred to as tropical tropopause layer (TTL) and is understood as the region of gradual transition from the troposphere to stratosphere.

[4] The physical processes occurring in the TTL are of great interest because the observed low concentrations of stratospheric water vapor can not be explained unless tropical tropospheric air entering the stratosphere through the TTL is dehydrated to stratospheric abundance of ~4 ppmv from ~13–20 ppmv [*Brewer*, 1949; *Dessler and Kim*, 1999; *Holton and Gettelman*, 2001]. The amount of water vapor in the stratosphere is important because it can affect stratospheric chemistry and radiative balance [*Kirk-Davidoff et al.*, 1999; *Forster and Shine*, 1999]. Since the traditional "freeze-drying" mechanism at the zonal mean TTL can not explain the stratosphere dehydration to the observed water vapor mixing ratio, *Newell and Gould-Stewart* [1981] proposed a "stratospheric fountain" hypothesis, in which the tropical tropospheric air enters the stratosphere preferentially in "cold" areas where the tropopause temperatures are below their annual and longitudinal mean values. The "fountain" region is mainly over the Western Pacific, with a little variation with season. However, later studies suggest that the Western Pacific can actually be an area with net subsidence at the tropopause [*Sherwood*, 2000; *Gettelman et al.*, 2000a]. *Holton and Gettelman* [2001] suggested that this paradox can be resolved by assuming that dehydration in the TTL is predominantly due to zonal horizontal transport of gradually ascending air through a "cold" region (e.g., Western Pacific). Ice crystals form and precipitate out of a given parcel in the region of coldest temperatures which it samples. As a result, the gradually ascending parcels entering the stratosphere at other longitudes (due to zonal horizontal transport) can be dehydrated to the very low saturation mixing ratios having characteristic of the "cold" region. This hypothesis implies, however, that tropopause temperature variations in areas other than the Western Pacific may also affect the entry value of water vapor mixing ratio from the troposphere into the stratosphere.

[5] Another hypothesized mode of dehydration of air entering the stratosphere involves deep convection overshooting in the TTL. As discussed in the work of *Johnston and Solomon* [1979], such convection would result in overshooting air masses adiabatically cool to much lower temperatures than the surrounding airs in the TTL. Rapid growth and sedimentation of ice particles in the convecting air masses could effectively remove much of the water in the air. This dehydration by overshooting convection is used by *Sherwood and Dessler* [2000, 2001] to model the stratospheric dehydration. Validation of this hypothesis for the control of stratospheric humidity requires measurements of small-scale humidity features associated with overshooting convection as well as the spatial and temporal distribution of these overshoots. In the past decade, several observational efforts have been made to map overshooting convection over both land and water near the tropics [e.g., *Hendon and Woodberry*, 1993; *Mapes and Houze*, 1993; *Liu et al.*, 1995; *Hall and Vonder Harr*, 1999; *Roach and Ramanathan*, 2000; *Soden*, 2000]. However, the relative importance of convective overshooting in the control of stratospheric humidity is still an open question.

[6] On the other hand, observational proof of *Holton and Gettelman*'s [2001] "cold-trap" hypothesis requires investigation of spatial and temporal variation of cold anomalies in the TTL and their relation to regions of low water mixing ratio. On a short time scale (hours to days), several observations suggest that the tropopause cold region is often correlated with strong convection. For example, *Johnson and Kriete* [1982] found a ~6 K cold anomaly near the tropical tropopause associated with local deep convection; *Teitelbaum et al.* [2000] found a simultaneous response of the tropical cold tropopause region to an incidence of deep convection. Recently, *Clark et al.* [2001] examined the 5-day evolution of MLS 68 hPa water vapor features during the dry phase of the atmospheric "tape recorder" [*Mote et al.*, 1996] and found they could not be explained by horizontal advection. On longer time scales (weeks to months), tropopause cold regions are affected by Kelvin waves [*Tsuda et al.*, 1994a; *Boehm and Verlinde*, 2000; *Holton et al.*, 2001]. The annual variation of the zonal TTL is mainly driven by extratropical stratospheric wind forcing, but some of the cold regional tropopause temperature anomalies can be seen as the response of the atmosphere to tropospheric diabatic heating/cooling due to convection [*Highwood and Hoskins*, 1998]. At even longer time scales (several years), the tropical cold tropopause region may be affected by ENSO [*Randel et al.*, 2000], volcanic eruption, solar cycle, and climate change. For example, a cooling trend of tropical cold tropopause region has been reported by *Zhou et al.* [2001] from the 1973–1998 sounding data. Most recently, *Read et al.* [2004] investigated interannual evolution of water vapor in the TTL measured by MLS. While not conclusively ruling out the importance of convective dehydration, their data show evidence of slow ascent of tropical water vapor between 12°S and 12°N zonal averages, and the result appears to be consistent with a simple model employing large-scale transport and freeze-drying in the cold region over the period of 1991–1993. On the other hand, *Randel and Wu* [2003] examined structure and variability of the tropical cold point tropopause using the observations of the Global Positioning System Meteorology

Experiment (GPS/MET) during 1995–1997 and found a significant correlation with the tropical deep convection as indicated by outgoing longwave radiations (OLR).

1.2. Gravity Waves Radiated From Deep Convection

[7] Another approach to study the characteristics of deep convection is to investigate the gravity waves (GWs) it radiates. From the modeler's point of view, GWs may be generated by deep convection due to (1) diabatic thermal forcing within the convective clouds, (2) ''obstacles'' to the flow produced by convective heating in clouds, or (3) ''mechanical'' oscillatory motions generated by a convective system [*Kim et al.*, 2003; *Fritts and Alexander*, 2003]. In the first two cases, the convection is made visible by clouds (i.e., ''moist convection''), while mechanical oscillatory motions could occur both in ''moist convection'' and in ''dry convection'' without the presence of clouds. In the real world, however, some combination of these three GW generation mechanisms may be present in any particular convective events. Properties that may govern GW generation in deep convection include: (1) the depth of diabatic heating layer, (2) the oscillation frequency of main updraft, and (3) the storm propagation speed [*Alexander et al.*, 1995]. Observations have show evidence of GWs in the tropics and subtropics that have a close correspondence with deep convective clouds [e.g., *Sato et al.*, 1995; *Dewvan et al.*, 1998; *Alexander et al.*, 2000]; however, the relative importance of different GW generation mechanisms remains to be seen [*Kim et al.*, 2003]. Several model studies in the past decade [e.g., *Fovell et al.*, 1992; *Goya and Miyahara*, 1998, 1999; *Lane et al.*, 2001] have argued that mechanical oscillation in the convection, no matter moist or dry, plays the most essential role for GWs generation. For example, *Lane et al.* [2001] calculated source terms of GWs generated by a mesoscale convection system (<100 km), and showed that a nonlinear effect due to the advection term of the Navier-Stokes equations dominates the GWs generation rather than the latent heating term or the eddy diffusion term. They thus concluded that mechanical oscillation of upward wind due to deep convection generates most of GWs at the level of neutral buoyancy around the top of deep convection [see also *Vadas et al.*, 2003].

[8] The characterization of differences between convection over land and convection over sea is another topic of research. Land and ocean have different specific heats. Tropospheric convection often occurs when a strong inversion layer of temperature appears. Land might play a role in heating the air and producing a temperature inversion layer in the lower troposphere in the daytime and thus affect the strength of the convection. However, future studies using more detailed observation and modeling will be required to distinguish between the GWs generated by oceanic convection from GWs generated by topographical convection.

1.3. Purpose of This Study

[9] In this paper, we investigate the convective scale perturbations in the TTL and their potential influence to stratospheric dehydration by studying the geographical distribution and temporal variation of tropical deep convection using a unique suite of data from UARS MLS. This suite includes water vapor, cloud radiance, and GW measurements. We focus on possible links between the low water vapor regions, low-temperature regions, high-altitude clouds, and their relation to the convection generated GWs. A brief description of the MLS data used in this study is given in section 2. The findings and analyses from these MLS observations are presented in two parts in section 3: one part focuses on the distribution and variation of water vapor, temperature, and cloudiness in the TTL; another focuses on the GWs in the stratosphere and how they are related to the former quantities in tropical deep convection events. Some preliminary modeling and other data support are presented in section 4. Concluding remarks are given in section 5.

2. MLS Measurements

[10] Launched on 12 September 1991, the UARS MLS measured limb atmospheric thermal radiation at 63, 183, and 203 GHz. Detailed descriptions of the orbital coverage, mission operations, and the major measurements of UARS MLS are given by *Waters et al.* [1999] and *Livesey et al.* [2003]. The following are brief descriptions of MLS products related to this study.

2.1. MLS Upper Tropospheric Humidity (UTH) Products

[11] Two upper tropospheric humidity (UTH) products have been developed by the MLS science team. V4.9 [*Read et al.*, 2001], derived from UARS 203-GHz radiances, provides water vapor mixing ratio and relative humidity with respect to ice from 467 to 147 hPa. More recently, V7.02 (W. G. Read et al., A new 147–68 hPa water vapor product from the UARS microwave limb sounder, submitted to *Journal of Geophysical Research*, 2004, hereinafter referred to as Read et al., submitted manuscript, 2004) has been developed to fill the gap between 147 hPa and the 100 hPa bottom of the 183-GHz stratospheric water vapor product, V0104 [*Pumphrey*, 1999]. The V7.02 data set is available from October 1991 to April 1993. These combined products give a continuous profile from 464 to 0.1 hPa with ~3–4 km vertical resolution. The estimated precision and accuracy for the V7.02 water vapor are ~0.1 ppmv and ~1 ppmv at 100 hPa, respectively.

2.2. MLS Cloud Radiance Measurements

[12] MLS cloud radiances are deduced from the UARS MLS 203 GHz radiances. As described by *Livesey and Wu* [1999] and *Wu and Jiang* [2002b], measured clear-sky 203-GHz radiances profiles as a function of scan angle are tightly clustered within bands given by the limits of water vapor variability. A simulated radiance profile using a clear-sky radiative transfer model [*Read et al.*, 2001], with 110% relative humidity (supersaturation in water vapor) throughout troposphere provides a limiting case for radiances which can be explained by water vapor variability in the absence of clouds (see also D. L. Wu et al., UARS MLS cloud ice measurements and implications for H_2O transport near the tropopause, submitted to *Journal of Atmospheric Science*, 2004, hereinafter referred to as Wu et al., submitted manuscript, 2004). Clouds at high tangent heights (higher than ~12 km) can produce radiances that are warmer than the 110% saturation limit and can be recognized and flagged. Similarly, clouds at low tangent heights (lower than ~6 km) can produce perturbations cold enough to be below the saturation limit and be detected. Such simulations using a

cloudy sky radiative transfer model are described by *Wu and Jiang* [2002b]. In some cases, the UARS MLS measured cloudy-sky radiances at 203 GHz can be ~20 K larger than the clear sky limit at high tangent highs or as low as <120 K below the clear sky limit at low tangent heights. In the middle tangent-height range between ~7 and ~11 km, clear and cloudy sky radiances are not so easily distinguishable. We define the cloud-induced radiance (K), or simply "cloud radiance," as the difference between the MLS measured cloudy sky radiance and the clear sky radiative transfer model calculated clear sky 110% saturated humidity limit at each tangent height. This model method for cloud detection in MLS measurements is described in detail by *Wu and Jiang* [2002b].

[13] In this paper, we use cloud radiances at high tangent heights of ~14 km and above (i.e., ≤147 hPa). At these tangent heights, the majority of the radiances observed by MLS originate from a region around the tangent point, which is the lowest point along a limb path. Only high-altitude clouds having cloud tops reaching within ~ ±1.5 km of that level can affect measured radiances. In other words, the cloud radiances at high tangent heights (≤147 hPa) are due to the presence of high clouds having altitude of ~12.5 km or higher. The clear sky radiative transfer model uncertainly is <2 K at ~147 to 68 hPa level near the tropics, and the MLS instrument noise for cloudy sky radiance measurements (at 203 GHz window channels) is <0.1 K (Wu et al., submitted manuscript, 2004). In this paper, we set the threshold of positive identification of cloud as >3 K in cloud radiance. Read et al. (submitted reference, 2004) recently validated this 3 K threshold by showing that with cloud radiances >3 K, the retrieved relative humidity are almost constant, indicating the atmosphere is cloudy and saturated. The cloudiness (%), or the cloud occurrence frequency, is defined as the ratio of total clouds flagged over the total number of samples.

2.3. MLS Gravity Wave Variances

[14] The MLS gravity wave (GW) variance is computed from the UARS MLS 63 GHz saturated limb radiance measurements near the bottom of each scan. Detailed descriptions of MLS GW radiance calculations and the recent improvements are given by *Wu and Waters* [1996a, 1996b] and *Jiang et al.* [2003, 2004]. These GW variances are available at eight altitudes (28, 33, 38, 43, 48, 53, 61, and 80 km) and are contributed mostly by waves of vertical wavelengths >10 km and horizontal wavelength of ~50–150 km. Recent studies using the MLS GW variances (some combined with model simulations) have related many of these GWs to the topography [*Jiang et al.*, 2002, 2003, 2004], convection [*McLandress et al.*, 2000] and possible jet-stream origins [*Jiang and Wu*, 2001].

[15] In this study, we use the recently improved four-point MLS limb-scan GW variances described by *Jiang et al.* [2003, 2004]. We focus on GW activity in tropical and subtropical regions and compare the GW maps and their seasonal variability with the MLS UTH and cloud radiance measurements.

3. MLS Observations and Analyses

[16] To understand the distribution of tropical convection and its relation to the transport of air into the TTL, we first investigate the cloudiness, temperature, and water vapor fields near the bottom (147 hPa), the midpoint (100 hPa), and at the top (68 hPa) of the TTL.

3.1. Cloudiness, Cold Tropopause Region, and Water Vapor Distributions in the TTL

[17] The black contour lines in Figures 1a, 1b, and 1c show the distribution of TTL cloud occurrence frequency, or cloudiness (%), as indicated on the contour labels. The MLS 203-GHz cloud radiance measurement is most sensitive to the clouds having ice water content greater than ~0.005 g/m^3 [*Wu and Jiang*, 2002b]. These dense high-altitude clouds seen by MLS are most likely to have been lifted by deep convection events (rather than the less dense thin cirrus which have smaller particle sizes), and their distribution is highly correlated with locations of vigorous convection activities. Regions of lowest TTL temperature (as indicated in the figure caption) are filled by the blue color. The green-colored areas are the regions with minimum V7.02 water vapor mixing ratio as indicated in the figure caption. Note at 147 hPa, the green color filled most of the region but left a white area near the tropics that shows the region of maximum water vapor concentration. Tropical wind profiles for the major convection centers are also plotted at the bottom panels of Figures 1a, 1b, and 1c.

3.1.1. December–March (Figures 1a and 1b)

[18] Near the bottom of the TTL at 147 hPa, there is a positive correlation between the centers of moisture maxima and the centers of high cloudiness. This correlation indicates cloud formation and rapid vertical transport of boundary layer water vapor in the deep convection. The region of lowest temperature at this altitude mainly resides from the south Indian Ocean to the Western Pacific, and its center is closely correlated to the bulk of the high cloudiness area. Note that at this altitude over the Western Pacific, the tropical winds are mostly westward directed (slightly northwestward) during this season, and the low temperature regions seem to be located slightly downwind from the convection center.

[19] At the higher altitude of 100 hPa, most of the low water vapor region (filled by the green color) is located northward of the tropical convection zone. The regions of lowest temperature (filled by the blue color) are somewhat correlated with convection centers but also seem to be shifted slightly northward relative to the high cloudy area. Such a displacement is similar to that seen in HALOE data by *Randel et al.* [2001].

[20] Near the top of TTL (68 hPa), the cloudiness frequency drops to a little above 2%, primarily located over the Western Pacific. At this altitude and above, the winds are mostly easterly (i.e., westward) jets. The low-temperature spots and a low water vapor region over the Western Pacific appear to be somewhat influenced by this wind pattern. Comparing the values of cloudiness at the bottom of TTL with those at the top, we estimate that about 5% of clouds that appeared at 147 hPa are lofted to as high as 68 hPa, and these very high altitude clouds are located mostly over the Western Pacific Ocean. Some caution should be taken in interpreting this as evidence that the deep convection penetrates to 68 hPa because the vertical smearing of the MLS data is about 3–4 km. Nevertheless, the lack of clouds at this level over the

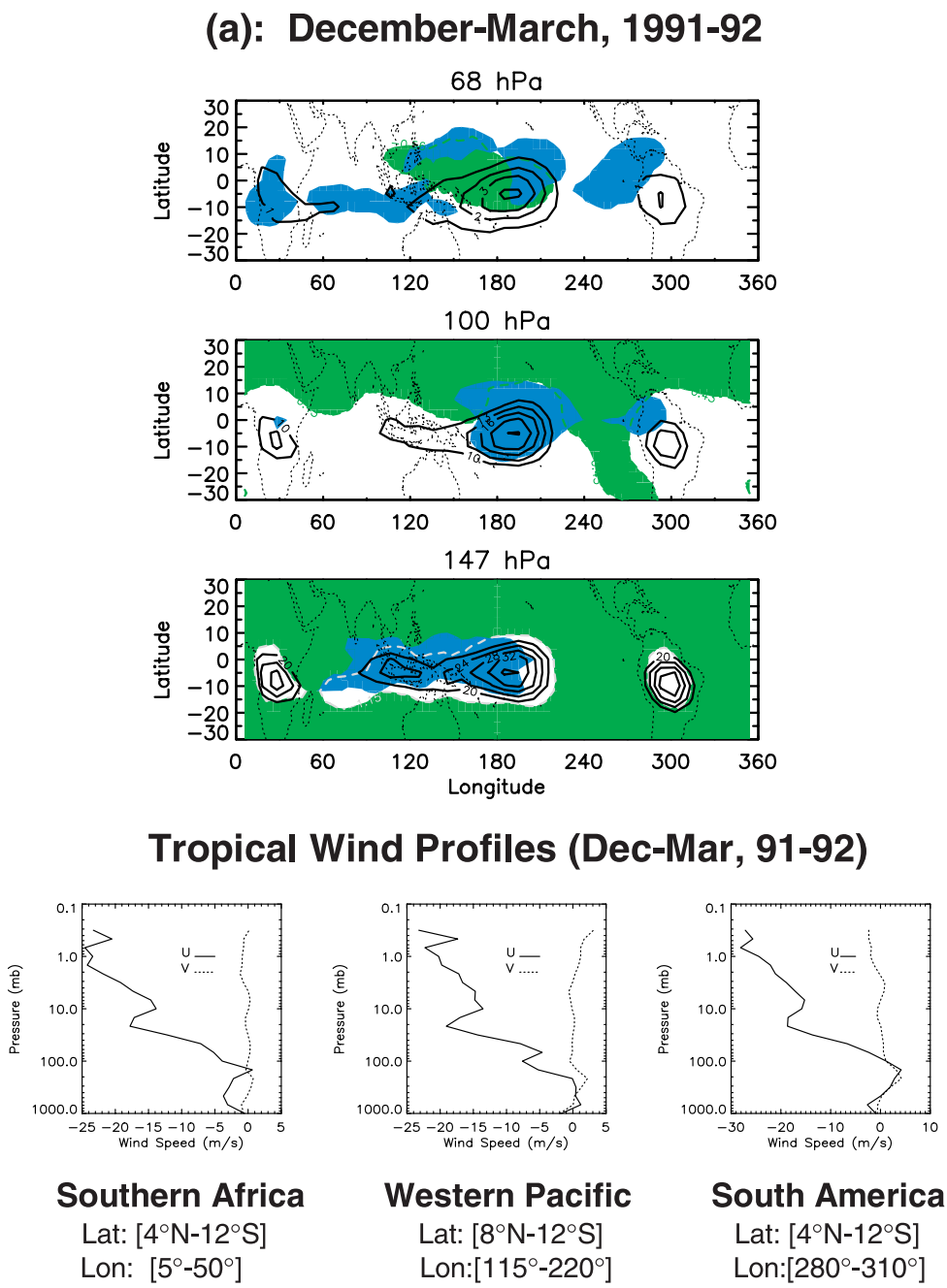

Figure 1a. Black line contours are the MLS measured cloudiness averaged for December–March 1991–1992 (the contour labels are values in %). At 147 hPa, 100 hPa and 68 hPa altitudes, only contours with cloudiness frequencies $\geq$20%, $\geq$10%, and $\geq$1% are shown, respectively. The green-colored areas are regions with the lowest value of v7.02 water vapor mixing ratio ($\leq$14.03 ppmv for 147 hPa, $\leq$2.67 ppmv for 100 hPa, and $\leq$3.60 ppmv for 68 hPa). The blue colors represent regions with the lowest temperature (≤ -68.0°C at 147 hPa, ≤ -79.3°C at 100 hPa, and ≤ -74.8°C at 68 hPa). The temperatures are computed from the UKMO (United Kingdom Meteorological Office) assimilated temperature data and averaged according to the UARS MLS measurement days. The lowest water vapor regions covered behind the lowest temperature plots are indicated by the dashed green lines. The data are averaged on $10° \times 5°$ longitude-latitude grids and a three-point smooth is applied to all the fields. Also plotted in the bottom panel is the UKMO mean wind (U, V) profiles for the three major convection centers.

African and South American continental regions might suggest that oceanic deep convection (such as those over the Western Pacific) is most capable of overshooting the tropical tropopause.

[21] It is also worth noting that the moisture behavior at 147 hPa is the inverse to that at 68 hPa, which might imply that a dehydration process occurs near the top of TTL above the convective sources. The fact that the center of minimum

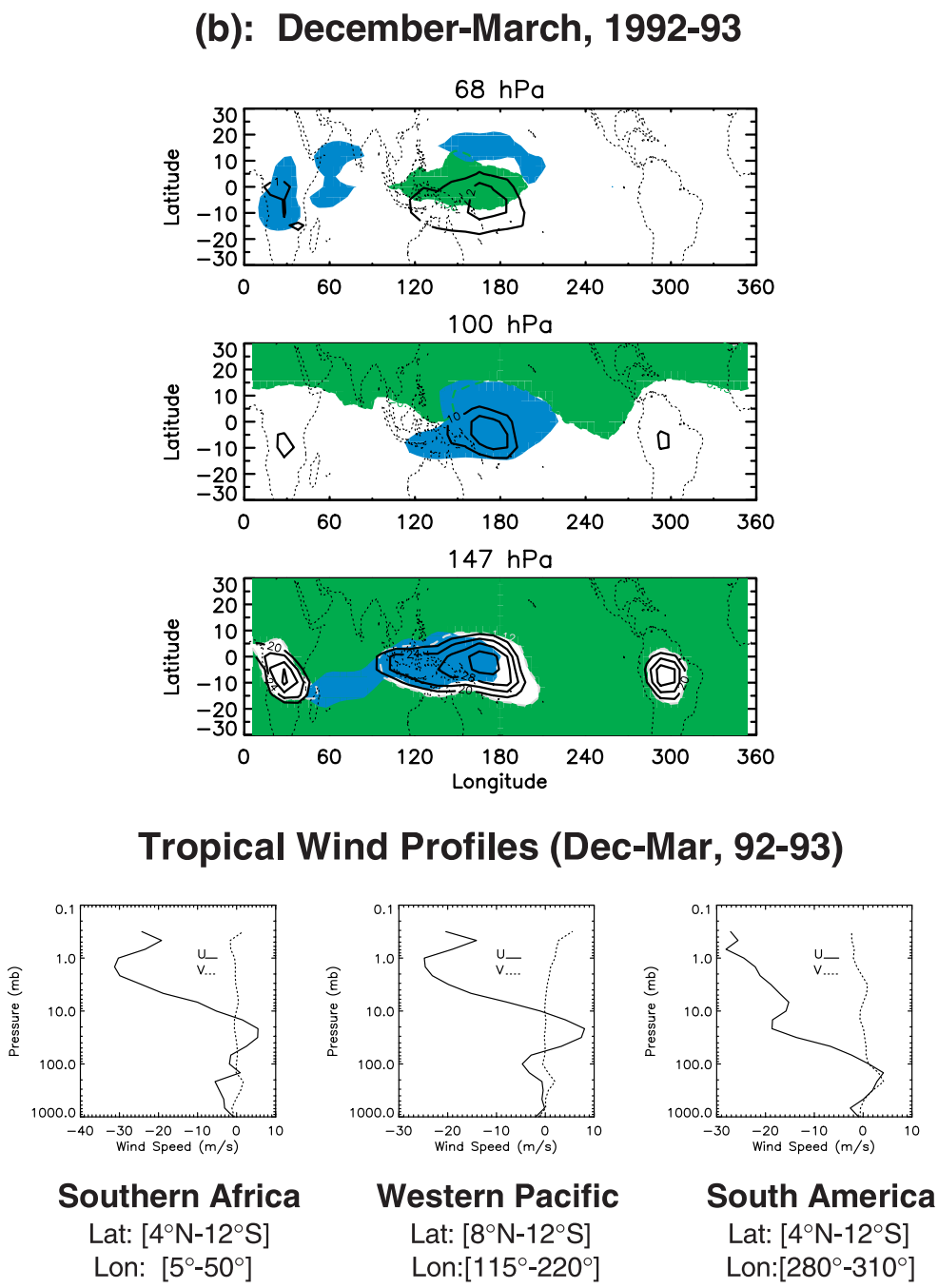

Figure 1b. Cloudiness contours and contour-labels are defined the same as in Figure 1a but for December–March of 1992–1993. The green-colored areas are regions with the lowest value of water vapor mixing ratio ($\leq$13.18 ppmv for 147 hPa, $\leq$2.67 ppmv for 100 hPa, and $\leq$3.60 ppmv for 68 hPa). The blue colors represent regions with the lowest UKMO temperature (≤ -68.7°C at 147 hPa, ≤ -79.3°C at 100 hPa, and ≤ -74.3°C at 68 hPa). Note the minimum values of water vapor and temperature used to draw the region boundary here is slightly different from that of Figure 1a, since our focus is the distribution of these minimum water vapor and temperature regions, not their actual values. The UKMO mean wind profiles are also shown for the major convection centers.

water vapor and temperature at 68 hPa is located slightly downwind of the deep convection also seems as a combination of "convective overshooting" dehydration process with rapid horizontal transport.

[22] The tropics of December–March of 1991–1992 (Figure 1a) appear to have more clouds in the TTL than they do in December–March of 1992–1993 (Figure 1b), a possible indication that there was more moisture entering the upper troposphere to form clouds in the 1991–1992 Northern Hemispheric (NH) winter/early spring than in the following year. Plausible reasons behind this include the impact of Mt. Pinatubo aerosol on cirrus clouds formation

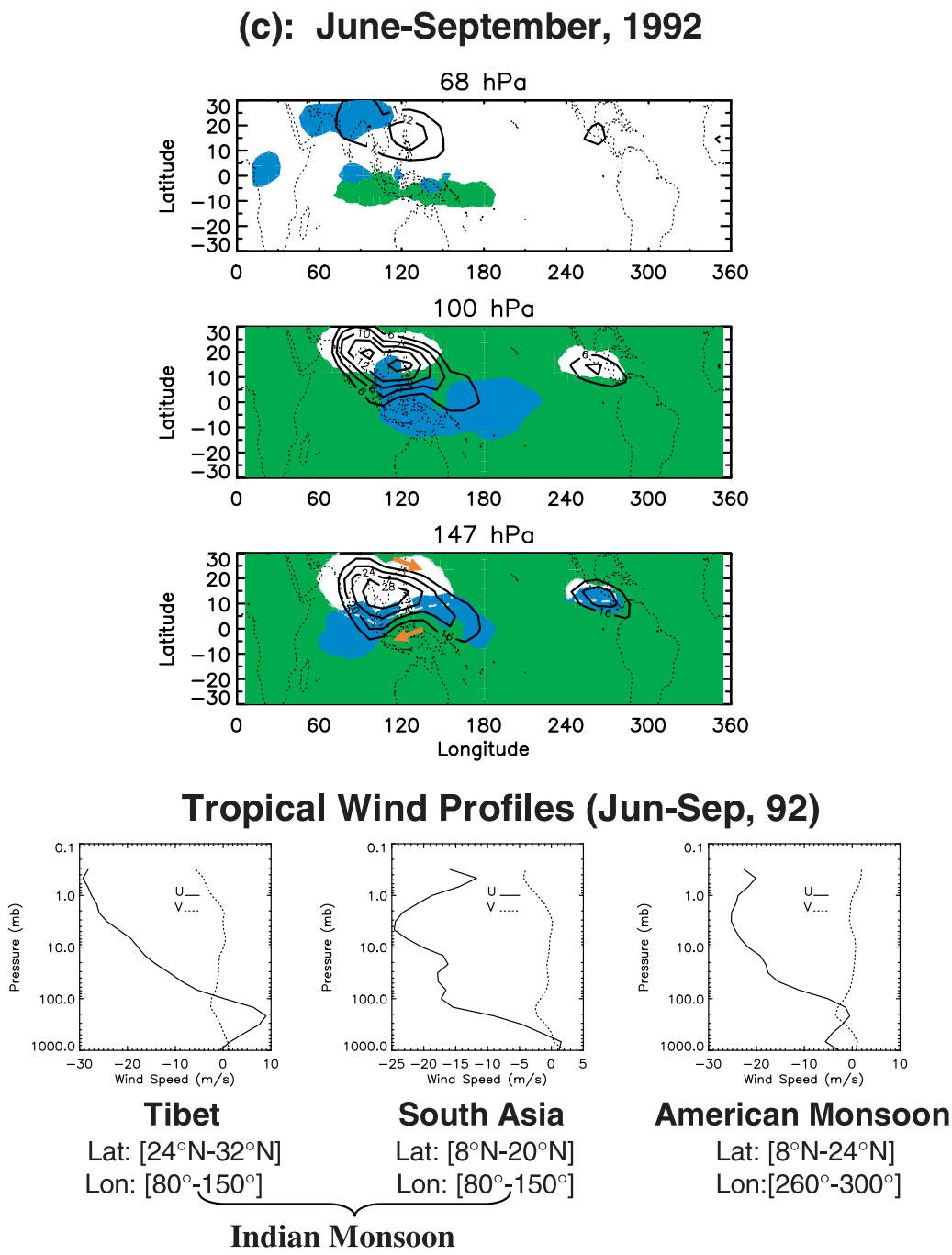

Figure 1c. Black line contours are the MLS measured cloudiness averaged for June–September of 1992. At 147 hPa, 100 hPa, and 68 hPa altitudes, only contours with cloudiness frequencies of 16%, 6%, and 1% are shown, respectively. The green-colored areas are the regions with the lowest value of water vapor mixing ratio ($\leq$16.03 ppmv for 147 hPa, $\leq$4.37 ppmv for 100 hPa, and $\leq$3.47 ppmv for 68 hPa). It is easier to see here that the white-colored areas uncolored by the green colors are the regions with high value of water vapor mixing ratios. The blue colors represent regions with the lowest UKMO temperature (≤ -68.4°C at 147 hPa, ≤ -75.8°C at 100 hPa, and ≤ -69.7°C at 68 hPa). UKMO mean wind profiles are also shown for the two major monsoon regions. The red arrows approximate the total wind directions.

[*Liu and Penner*, 2002; *Lohmann et al.*, 2003] and the influence of ENSO to tropical climate [*Massie et al.*, 2000; *Jensen et al.*, 1996].

3.1.2. July–September (Figure 1c)

[23] During NH summer to early fall (Figure 1c), there are two regions of high cloudiness and high water vapor in the TTL. The largest one that stretches from Tibet/South China to South/Southeast Asia is possibly related to the Indian monsoon. The winds at ~147 hPa (and lower altitudes) over Tibet blow mostly eastward (slightly southeastward), while the winds over South Asia are mainly westward (slightly southwestward). The low temperature

region at this altitude mostly occurs near the southern edge of this huge anticyclonic wind pattern (as indicated by the red arrows) at 147 and 100 hPa. Over this extended Indian monsoon region, an estimated 5% of the clouds at 147 hPa reach as high as 68 hPa where the winds become mostly westward. The region of minimum water vapor at the top of TTL (68 hPa) appears in the equatorial zone mostly over the Indian Ocean to Western Pacific, while the minimum temperature regions are scattered around west to south of the India monsoon. The Central American monsoon is much smaller in scale but is clearly correlated to a small ''cold spot'' at the 147 hPa bottom of the TTL.

[24] It is worth to note that the two regions of maximum moisture at both 147 hPa and 100 hPa are associated with the high cloudiness over Indian and American monsoons. This moisture behavior is not clearly reversed at the top of TTL as it does during the December–March season, suggesting that convection over the land masses might actually be acting to moisten the air in the TTL, rather than dehydrate it.

[25] The new V7.02 water vapor data that is used to plot the maps in Figures 1a, 1b, and 1c is not available for the summer of 1993, but our analyses found that the low-temperature areas (not shown here) distributed in 1993 summer are more or less the same pattern as those in the 1992 summer. Also note is that there seems to have less TTL cloudiness during the NH summer than during the NH winter (compare the values labeled on the cloudiness contour). This indicates that maximum cloudiness in the TTL occurs during the NH winters or Southern Hemisphere (SH) summers, when the tropopause is highest and coldest. (Also see Figure 8 in the later section for comparison between time series of cloudiness during NH and SH summers.)

3.2. Stratospheric Gravity Waves Above the TTL

[26] While much attention has been paid to the temperature and moisture in the studies of TTL dehydration, clear correlation between deep convection and enhanced GW activity has been observed, particularly in the tropics [e.g., *Karoly et al.*, 1996; *Tsuda et al.*, 1994b, 2000; *Alexander et al.*, 2000; *Preusse et al.*, 2001]. In some cases, GWs associated with convection can feed back to modify or reorganize severe deep convection and precipitation [*Koch and Siedlarz*, 1999]. Thus knowledge of how GWs propagate upward above the tropopause in background winds and how their distribution and time evolution is linked to climate conditions can yield rich information about convection near the tropics.

3.2.1. Effect of the Background Winds

[27] Let us first look at how GWs propagate upward in the background winds. GWs generated by deep convection usually have short periods and thus the linear theory can be applied [*Salby*, 1996]. To assess the influence of background winds on the vertically propagating GWs, the following dispersion relationship derived from a nonhydrostatic, compressible, two-dimensional (2-D) fluid equation system is useful when the effect of background winds is taken into account:

$$m^2 = \frac{N^2}{(\bar{u}-c)^2} + \frac{k^2(\bar{u}-c)^2}{c_s^2} - k^2 \qquad (1)$$

where k denotes the horizontal wavenumber, m denotes the vertical wavenumber, $\bar{u}$ denotes the zonal mean wind velocity, c denotes the horizontal phase velocity, c_s denotes the sound velocity, and N denotes the buoyant frequency. For $m^2 > 0$, the solutions for the basic equations have a sinusoidal form in the vertical direction and are referred to as internal. The amplitude of the GWs is proportional to $\exp(z/(2H))$, where H is the scale height. *For* $m^2 = -m'^2 < 0$, the solutions become $\exp(-m'z)$ in the vertical direction and the phase becomes constant with height and are referred to as external. Even though their energy decreases with height, external waves in the range $1/(2H) > m'$ amplify upward like $\exp[(1/(2H) - m')z]$ due to stratification of the background atmosphere. On the other hand, they damp upward in the range $1/(2H) < m'$.

[28] Environmental conditions determine N, c_s, and $\bar{u}$. Physical aspects of the convection control the GWs spatially and temporally (as mentioned in section 1). Thus k and c are determined by the convective source. Finally, the vertical wavenumber m may be determined. According to equation (1), it is found that the static stability N^2 mainly contributes to the positive part of m^2. Since k^2 reduces m^2, GWs with short horizontal wavelength cannot propagate vertically for a particular k. Vertical propagation is strongly controlled by the intrinsic phase velocity $c - \bar{u}$. Thus when GWs generated by convection vertically propagating through the shear wind zone, filtering due to the background wind happens. For example, when $\bar{u} \sim 40$–50 m/s, assuming $N \sim 0.02$ rad/s, the vertical wavelength of GW can be estimated as $\lambda_z \sim 13$–16 km, which is within the MLS filter range. Conversely, if the value of $\bar{u}$ is small or negative it could result in the GWs having too short a vertical wavelength to be visible by MLS.

[29] The effect of filtering by the background wind, as described above, can be best illustrated by Figure 2, which shows measured MLS zonal mean GW variances in January 1992–1994 (left) and July 1992–1994 (right) in comparison with CIRA zonal wind climatology [*Fleming et al.*, 1990]. The GW variances exhibits a slight tilt with increasing height similar to the stratospheric and mesospheric jets, which are tilted southward with height in SH summer (January) and tilted northward with height in NH summer (July). In January, at latitudes of ~50°N to ~70°N, orographic mountain waves [*Jiang et al.*, 2003, 2004] and jet stream-induced waves are the major GWs seen by MLS; at latitudes of ~5°S to ~25°S, convection-induced GWs [*McLandress et al.*, 2000] are the primary sources. In July, the wave sources at latitudes of ~40°S to 70°S are likely the combination of mountain waves from the southern Andes, Drake Passage, and the Antarctic rim [*Jiang et al.*, 2002, 2003; *Wu and Jiang*, 2002a]. At latitudes around 25°N, the GW sources are primarily from subtropical deep convection. The lowest zonal GW variances are observed around the zero wind lines above the tropics.

3.2.2. GW Variance Maps

[30] We now turn our attention to the distribution of GWs above the TTL. Because of the background wind filtering effect discussed above, the center of maximum GWs at higher altitude shift slightly southward in SH summer and northward in NH summer relative to the GWs at lower altitude, as shown by the two examples in Figure 3, in which GWs at 28 km (black contour lines) and at 38 km

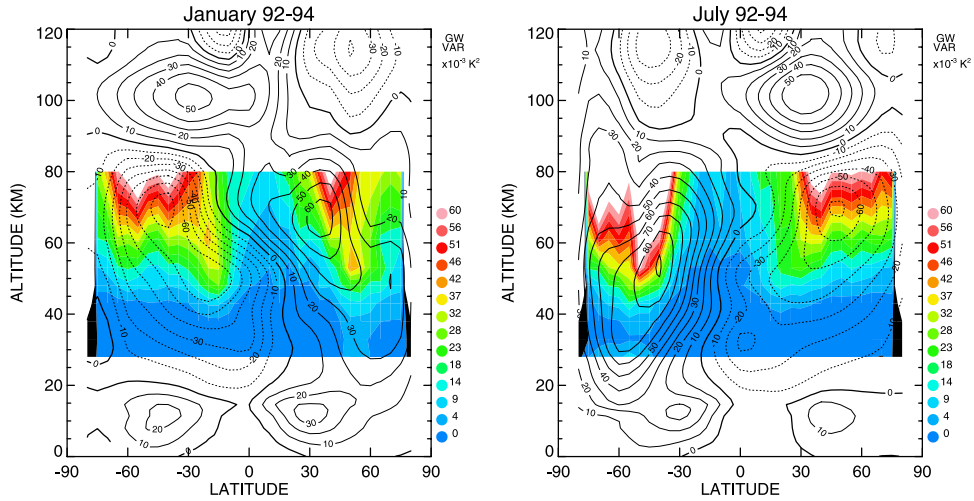

Figure 2. This diagram shows MLS zonal mean GW variances (color-filled contours) for January 1992–1994 (left) and July 1992–1994 (right), in comparisons with the CIRA (COSPAR International Reference Atmosphere) zonal wind climatology [*Fleming et al.*, 1990]. The black solid lines show easterlies, and dotted lines are westerly winds. The instrument noises have been removed from the GW variances. Note that in both summer hemispheres the GW variances shift poleward when propagating upward into the stratosphere.

(color-filled contours) are both plotted. In summer hemispheres, the background stratospheric winds are usually greater than ~30 m/s at altitudes ≥38 km above the subtropical convection zones, thus GWs are mainly detectable by MLS at this height (~38 km) and above (see Figure 2). Occasionally, MLS also detects the GW signals as low as ~28 km, such as during December–March of 1991–1992 (Figure 3, top panel) and June–September of 1994 (Figure 3, bottom panel). In other years/seasons, e.g., December–March of 1992–1993, GWs at 28 km are mostly undetectable by MLS due to unfavorable wind conditions. Thus to compare GW distribution with TTL cloudiness map, we will focus on the MLS GW maps at 38 km, where the GW is detectable for all 1991–1994 NH winters and summers. Figures 4a and 4b show the maps of such comparison. In these maps, GWs are shown by the color-filled contours, where the V4.9 relative humidity with respect to ice (*RHi*) at 147 hPa (shown as the black contour lines) and the MLS measured cloudiness (%), also at 147 hPa (shown as the white contour lines), are overplotted. (The reason that we use the V4.9 *RHi* in these maps rather than the V702 is that V4.9 data cover a longer time period comparable to the time period of the MLS GW measurement). For readability, only contour values with $RHi \geq 90\%$ and cloudiness ≥20% for December–March and $RHi \geq 80\%$ and cloudiness ≥15% for June–September are shown.

[31] The most obvious feature in the Figure 4 is that the maximum GW activity areas, due to the background wind filtering effect, are located poleward of the centers of cloudiness. Also, the centers of TTL cloudiness are slightly drifted westward (or downwind) of the active GW regions, especially in the NH winters/SH summers. Nevertheless, MLS observations show that during the NH winter and early spring (December to March), strong GW activities seem to correlate with the tropospheric deep convection zones in the tropics (see color-filled contours in Figure 4a). These activities are centered at Southern Africa, Western Pacific, and South America. In previous analyses of MLS data [e.g., *Wu and Waters*, 1996b; *McLandress et al.*, 2000], the variances were smoothed over a large area to improve the GW signal-to-noise ratios. As a result, it was only possible to visualize planetary-scale features. With the recently improved four-point limb-scan variances [*Jiang et al.*, 2003, 2004] that are used in this study, more details on convection-induced GWs can be seen. For example, some of the convection-related GWs could be correlated with topographic features including small islands in the south Pacific. Also, the storm systems over the oceans are seen to generally produce weaker GW variances compared to those hitting the east side of land masses. During the NH summer to early fall (June–September) the GW variances show strong wave activities over the northern subtropics, including major wave activities in North Africa, Southern Asia, and Central America (see color-filled contours in Figure 4b). Note also that the expected stronger correlation between regions of high cloudiness and high *RHi* is evident in these data (both in Figures 4a and 4b).

3.2.3. MLS Inferred Wave-Propagating Direction

[32] The GW variance maps shown in Figure 3 and 4 are averaged over MLS north-looking ascending (NA) and south-looking descending (SD) orbits. (Detailed description of different MLS orbits and observation models can be found in the works of *Jiang et al.* [2003, 2004] and *McLandress et al.* [2000] and are therefore not discussed here). This is because the MLS GW variances are very sensitive to the wave propagation direction [*Jiang and Wu*, 2001; *Jiang et al.*, 2003, 2004]. For the convective cases, we found that variances are much stronger when observed on NA or SD orbits than they were measured on north-looking descending (ND) or south-looking ascending (SA) orbits (see examples in Figure 5). In the tropics and low-latitude subtropics, the MLS line-of-sight (LOS) is mostly pointing west and is scanning from top to surface when in the NA or SD observing modes. The fact that much stronger

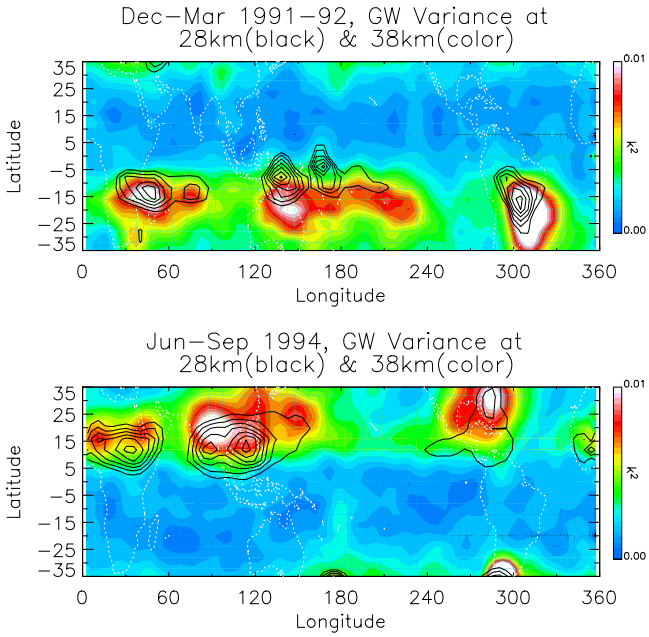

Figure 3. Color-filled maps are the MLS limb scan GW variances at 38 km altitudes averaged for December–March of 1991–1992 (top), and July–September 1994 (bottom), respectively. The GW variances are averaged using measurements from the UARS MLS north-looking ascending and south-looking descend orbits. The black contours are the same GW variances but computed for lower altitudes at 28 km (contour level range is 0.002–0.005 k^2). Instrument noises for both altitudes have been removed. Note the centers of the GW activities at 28 km are closer to convection sources near the equator than the GWs at 38 km. The data are averaged on $10° \times 4°$ longitude-latitude grids and a three-point smoothing is applied to smooth the fields.

GW signals are observed in these two observing modes implies that downward propagating wave fronts must be tilted toward the east (as shown in Figure 6). (This is different with the wave-front travel direction of wintertime orographic "mountain waves" described by *Jiang et al.* [2004]. The MLS observed mountain wave variances are strong in ND and SA modes, which implies that the wave-front is tilted toward the west). In the subtropics of both north and south summer hemispheres, the stratospheric jets are predominantly westward winds. As illustrated in Figure 6, the propagation direction of convection generated gravity waves observed by MLS is tilted in such way that the horizontal component of the wave vector $\mathbf{k_h}$ is opposite to the wind vector **U**. The other "half" of the waves with $\mathbf{k_h}$ traveling in the same direction as **U** is "dead," or "filtered out" in the background winds. In other words, the GWs observed by MLS are dominated mostly by the downward phase propagating waves having horizontal phase velocities opposite to the stratospheric jet streams. This is in agreement with the numerical model simulations [e.g., *Goya*, 1998; *Goya and Miyahara*, 1998; *Lane et al.*, 2001], which show that vertical propagating GWs generated by convection expand to a fan-like region and spread horizontally with height in the direction facing the background wind. The NA and SD MLS viewing directions, depicted as direction B in Figure 6, are favorable for resolving the wave patterns generated by convection because it intercepts the wave roughly parallel to its tilted wave fronts.

3.2.4. MLS Observed Vertical Growth of GWs

[33] Figure 7 shows mean vertical profiles of GW variances normalized by mean radiance brightness temperatures, derived from the 3-year limb scan measurements above the major SH and NH summer convection centers in the subtropics. These profiles show that convection-generated GWs grow exponentially when they propagate through the stratosphere. This is consistent with earlier zonal mean profiles shown in Figure 2. Below ~50 km, the growth rates closely follow the nondissipating rate $\sim\exp(\int dz/H)$, where $H \sim 7$ km is the scale height [*Fritts and VanZandt*, 1993]. At altitudes above ~50 km, the growth rate becomes smaller, possibly due to wave dissipation/saturation [*Wu*, 2001] or wind-modulated apparent "saturation" in MLS variances [*Alexander*, 1998].

3.2.5. Seasonal and Interannual Variation

[34] As to the seasonal and interannual variability in the tropics, *Gettelman et al.* [2000b] reported a declining trend of MLS V4.9 relative humidity (and therefore cloudiness) in the 1991–1994 time period. They have shown a minimum relative humidity but maximum temperature between 147 and 215 hPa in 1994, as well as a shallow maximum of water vapor mixing ratio at the same level. Although several possible mechanisms that could cause this anticorrelation of temperature and cloudiness during this time scale were discussed in their report (e.g., Pinatubo eruption, El Nino and La Nino events), there was no firm conclusion to this question.

[35] In previous sections, we have shown that deep convection is highly localized events. The seasonal and interannual evolution of localized convection can be assessed using 30-day running means of the TTL cloudiness and of the convection-generated GW variances above the major convection centers, as shown in Figure 8. During the period of 1991–1994, MLS cloudiness (measured using 203 GHz) and GW variance (measured using 63 GHz) are almost continuously observed. After November 1994, however, the data are more intermittent and sparse. Especially between December 1994 and August 1995, the limb-scan dataset that is used in this study has large gaps. The MLS scan pattern was also changed from normal scan (i.e., from top-of-atmosphere to surface) to reverse scan (from surface to top-of-atmosphere) after 1994. Details of differences between these two observation modes, especially for GW measurements, are yet to be investigated [*Jiang et al.*, 2003]. Thus in this paper, we mainly focus on our discussions to the "good" period of 1991–1994 and leave the reverse scan period (1995–1997) to future studies.

[36] Figure 8a shows a somewhat decreasing trend of the 100 hPa cloudiness in 1991–1994, for all the three SH summertime (i.e., NH wintertime) convection-active regions (Southern Africa, Western Pacific, and South America). However, there is little evidence of decrease in the frequency or strength of the tropical/subtropical deep convection found in the 38 km GW variances (Figure 8b) during the same period, although we can not completely rule out such possibility since GW strength is also determined by the background winds and further modeling studies are required. For the two dominant convection sources in NH summer

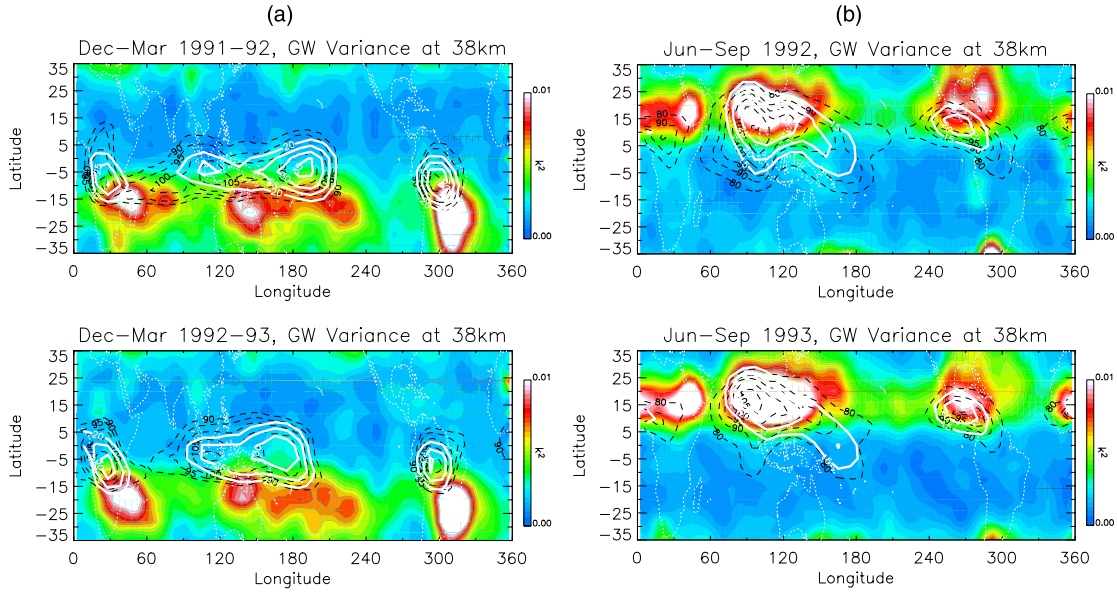

Figure 4. (a) The color-filled maps are the mean MLS limb-scan GW variances at 38 km for December–March of 1991–1992 (top) and 1992–1993 (bottom), respectively, and averaged using data taken from UARS MLS north-looking ascending and south-looking descend orbits. The instrument noise has been removed. The white contours are the MLS measured cloudiness (%) at 147 hPa. Only contours with cloudiness frequency $\geq$20% are shown. Black contours are relative humidity (*RHi*), also at 147 hPa. Only contours with *RHi* $\geq$ 90% are shown. The data are averaged and smoothed using the same method as in Figure 3. (b) Same as in Figure 4a except the fields are averaged for July–September of 1992 (top) and 1993 (bottom), respectively. Only contours with cloudiness frequency $\geq$15% are shown. Black contours are relative humidity (*RHi*), also at 147 hPa. Only contours with RHi $\geq$ 80% are shown.

(Indian monsoon and American monsoon regions), the deep convection in the Indian monsoon area seem to generate more high clouds (Figure 8d) in the TTL and stronger GW variances (Figure 8e) in the stratosphere (although strictly speaking, one cannot compare the strength between the two centers of convection using Figure 8 since the GWs and cloudiness in the two cases are averaged over different areas). However, comparing the three NH summers in 1992–1994, there is neither a clear decreasing nor increasing trend in either the TTL cloudiness or the stratospheric GW variances.

[37] It is also interesting to note that the peaks of the TTL cloudiness are much broader than those of the stratospheric GW variance. This can be explained by the background wind filtering processes. Figures 8c and 8f show the stratospheric background U winds at vicinity of ~38 km. The anti-correlation between the GW "peaks" and U wind "valleys" (as indicated by gray arrows) suggests that most GWs radiated from deep convection can propagate upward into the stratosphere only when the background winds are westward (U < 0). The apparent increasing trend of TTL cloudiness during period of 1995–1997 and its relation to the GW variance will be investigated in a separated study and thus are not discussed here.

4. Other Preliminary Modeling and Data Analyses

4.1. Topography Disturbances Simulated by MWFM

[38] In order to see whether some of the TTL disturbances and stratospheric GWs seen by MLS are actually topographically forced mountain waves (MWs), the Naval Research Laboratory Mountain Wave Forecast Model (MWFM 2.1) is used to simulate the stratospheric temperature perturbations produced by upward propagating orographic MWs near the tropical and subtropical regions. The MWFM 2.1 is described in detail by *Jiang et al.* [2002, 2004]; a brief description is given here. MWFM blows atmospheric winds over digital representations of the Earth's major topographical features and calculates a spectrum of forced mountain waves. The model simulates subsequent propagation of these waves according to vertical profiles of winds and temperatures and keeps track of the waves' amplitudes along the way [*Broutman et al.*, 2001]. The background temperature and wind fields are taken from the United Kingdom Meteorological Office (UKMO) assimilated meteorological data. The ray equation in MWFM 2.1 is governed by a nonhydrostatic dispersion relation with rotation and density scale height according to *Marks and Eckermann* [1995].

[39] Figure 9 illustrates the MWFM 2.1 simulated MW activities at 5 hPa (~37 km) for both SH summer (left) and NH summer (right). In both the winter and summer cases, the model results show strong subtropical orographic MW activities over the mountain ridges of northern India, Middle East, and Mexico. However, recent modeling studies using a sophisticated MLS filter [*Jiang et al.*, 2004] indicated that due to unfavorable stratospheric wind conditions over the northern subtropics during SH summer, MWs over these regions have "wind-filtered" vertical wavelengths of <10 km and thus

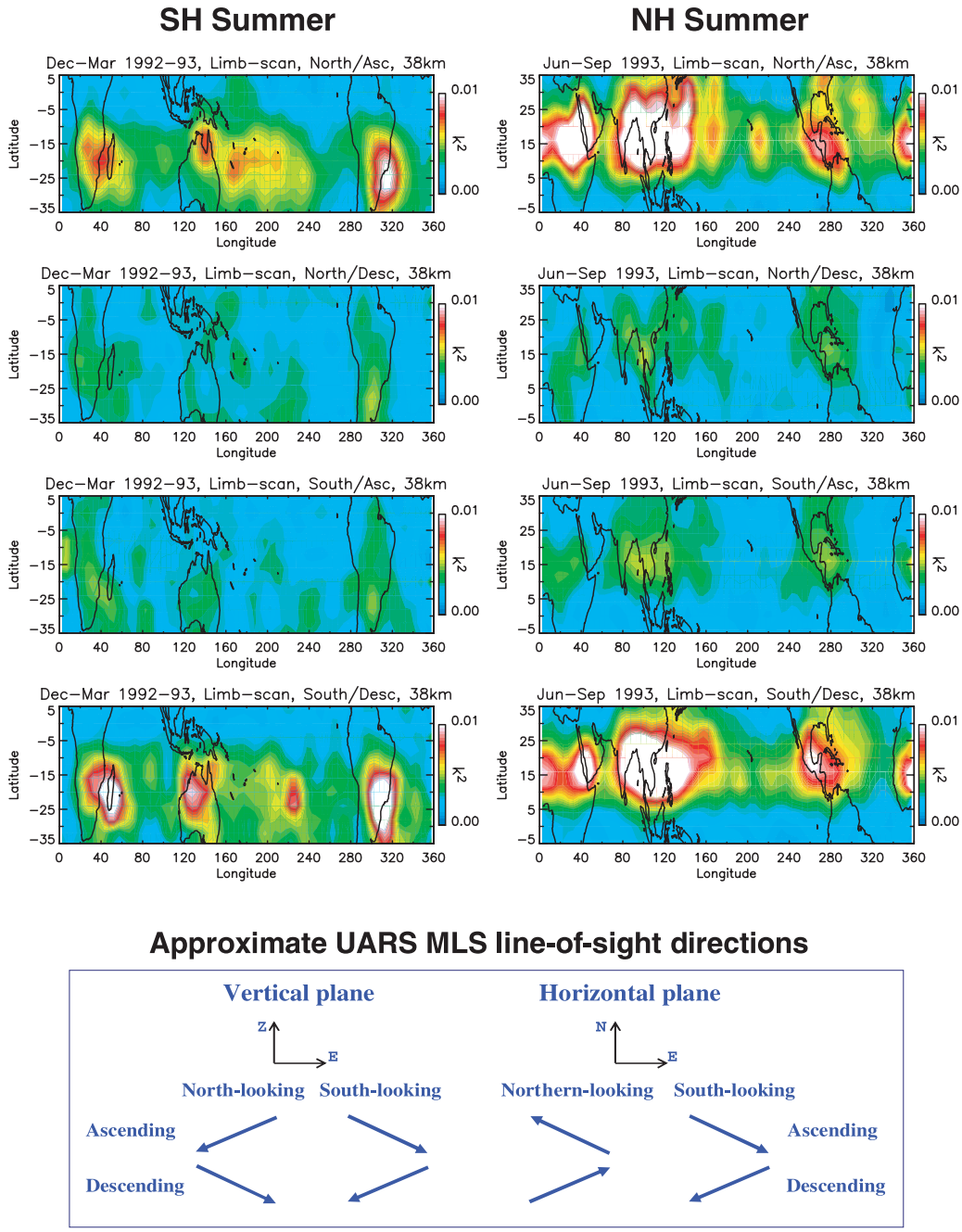

Figure 5. Examples of MLS GW variances measured from different observational modes. (left column) December–March of 1992–1993; (right column) July–September of 1993. (first row) Data from north-looking ascending orbits; (second row) north-looking descending orbits; (third row) south-looking ascending orbits; (fourth row) south-looking descending orbits. Note the convection generated GWs produce stronger signals detectable by MLS on north-looking ascending (first row) and south-looking descending orbits (fourth row), when the MLS LOS is looking mostly westward and is scanning the atmosphere from top to surface. The approximate MLS line-of-sight directions for different observation modes are shown at the bottom panel.

are unlikely to be seen by the MLS. During the NH summer, however, substantial wave activities over northeast Africa and Mexico might be seen by MLS. A study by *Goya* [1998] using a 2-D nonhydrostatic model showed that stratospheric GWs generated by deep convection could have vertical wavelengths of >13 km, which is within the MLS filter range. Thus with the MWs being ruled out, MLS measured GW activities in tropical and subtropical regions during the SH summer/NH winter (December–March) indicate strong convective activities in these regions. During the NH summer (July–September), subtropical wave turbulences seen by MLS

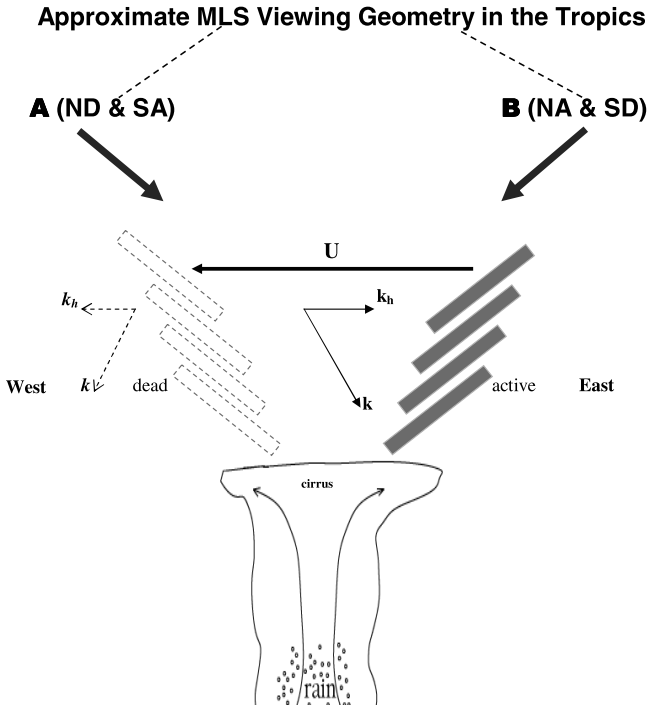

Figure 6. This diagram illustrates the MLS inferred deep convection generated GW wave-front propagation direction. Note only the wave fronts at "east half" of the convection have horizontal components of the wave vector $\mathbf{k_h}$ opposing to the wind vector **U**. The other "west half" of the waves with $\mathbf{k_h}$ traveling in the same direction as **U** are "dead" or filtered out by the background winds. Two approximate MLS viewing geometries near the tropics are shown above the convective waves. Viewing geometry B is most favorable for resolving this wave perturbation in saturated MLS limb scan radiances.

might be mixed with both convection and topography generated GWs.

4.2. Convective Perturbations From ECMWF Wind and NOAA OLR and CMAP Rainfall Analyses

[40] From the MLS observations of stratospheric GWs and upper troposphere cloudiness described in the previous sections, it is obvious that deep convection near the tropics seem to occur in preferred regions. To see if the wind fields, OLR, and rainfall patterns agree with the MLS data, we show in Figure 10 the maps of 150 hPa monthly mean wind (top row), velocity potential, and divergent wind (second row) derived from the European Centre for Medium-Range Weather Forecasts (ECMWF) gridded global analysis. The data are averaged for January 1992–1994 (left column) and July 1992–1994 (right column) to illustrate both SH and NH summers. Also shown in the third and fourth rows in Figure 10 are the OLR map obtained from the NOAA Climate Diagnostics Center and the precipitation pattern derived from the NOAA Climate Prediction Center Merged Analysis of Precipitation (CMAP); both the OLR and CMAP date are also averaged for January 1992–1994 and July 1992–1994. The OLR data have been widely used to indicate regions of deep convection [e.g., *Motell and Weare*, 1987; *Horel et al.*, 1989; *Murakami and Wang*, 1993; *Mitchell and Wallace*, 1992]. The CMAP blends station rain observations and five different types of satellite products to estimate global precipitations [*Huffman et al.*, 1997; *Xie and Arkin*, 1997]. In general, the CMAP and OLR data share common patterns. Low OLR centers correspond to high precipitation centers extremely well, although CMAP tends to include more small-scale details [*Wang*, 1994a, 1994b].

[41] The January 150 hPa wind field reveals the dominance of strong westerlies over subtropics both north and south of the equator. In the deep tropics, the easterlies associated with SH summertime monsoon prevail over the maritime continent, Western Pacific, and equatorial Africa;

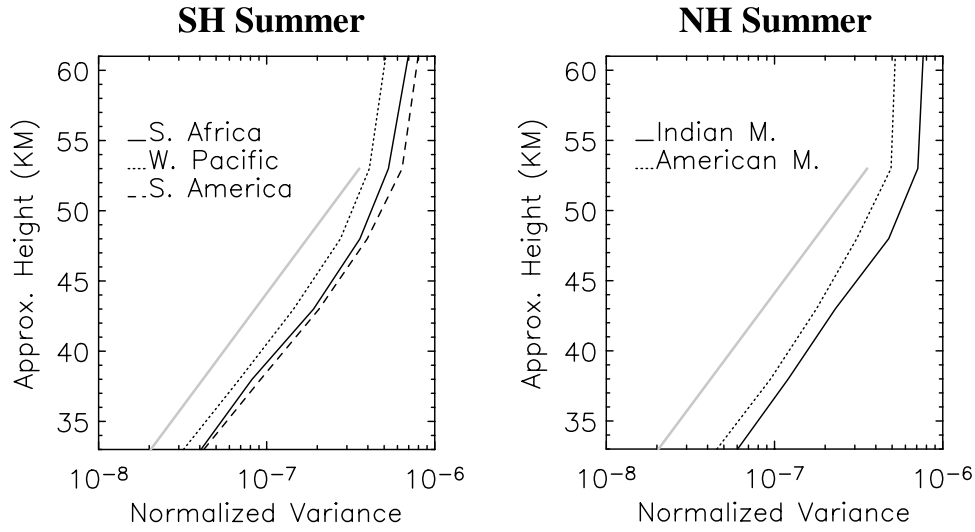

Figure 7. Vertical growth of normalized MLS GW mean variances over the major convection for December–March 1991–1994 (left) and June–September 1992–1994 (right) as observed on NA and SD orbits. The instrument noise was removed from these variances. The gray curve shows sample $\exp(\int dz/H)$ growth with $H = 7$ km.

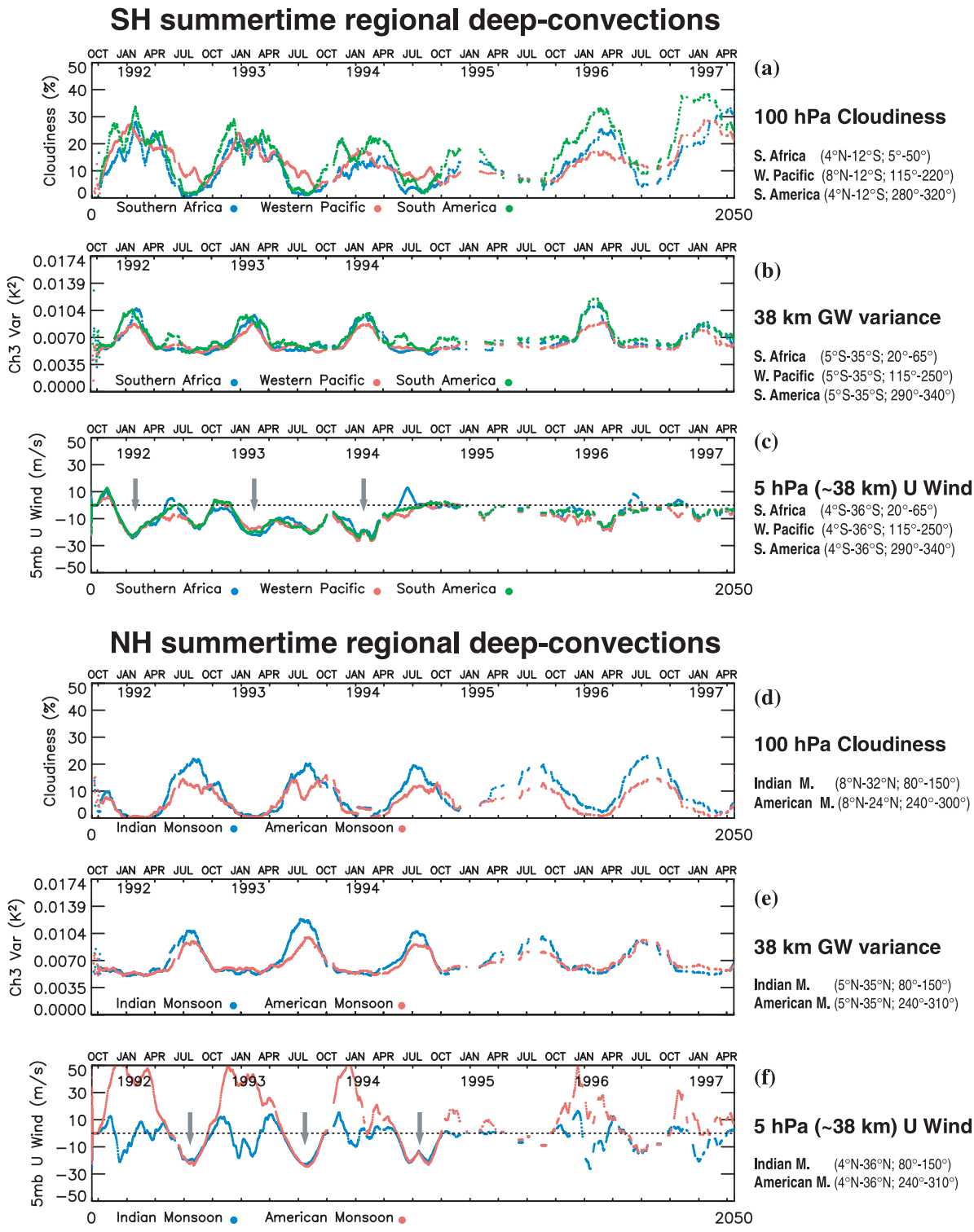

Figure 8. Time series of 100 hPa cloudiness, 38 km GW variance, and stratospheric background U wind. All data are zoom-averaged above the most dominant regional convection, and are 30-day running window means of the daily values. (a and b) Cloudiness and GW variance for three dominant SH summer-time convection regions of Southern Africa, Western Pacific, and South America; (d and e) Cloudiness and GW variances for the two major NH summer-time convection, Indian Monsoon and American Monsoon. The latitudes and longitudes between the cloudiness and GW variances plots are slightly different for most of the convection regions, because the GW maxima are shifted following the stratosphere wind pattern as discussed in the text. The U winds (c and f) are averaged between 4.6 to 6.8 hPa levels that are approximately the background of ~38 km GWs.

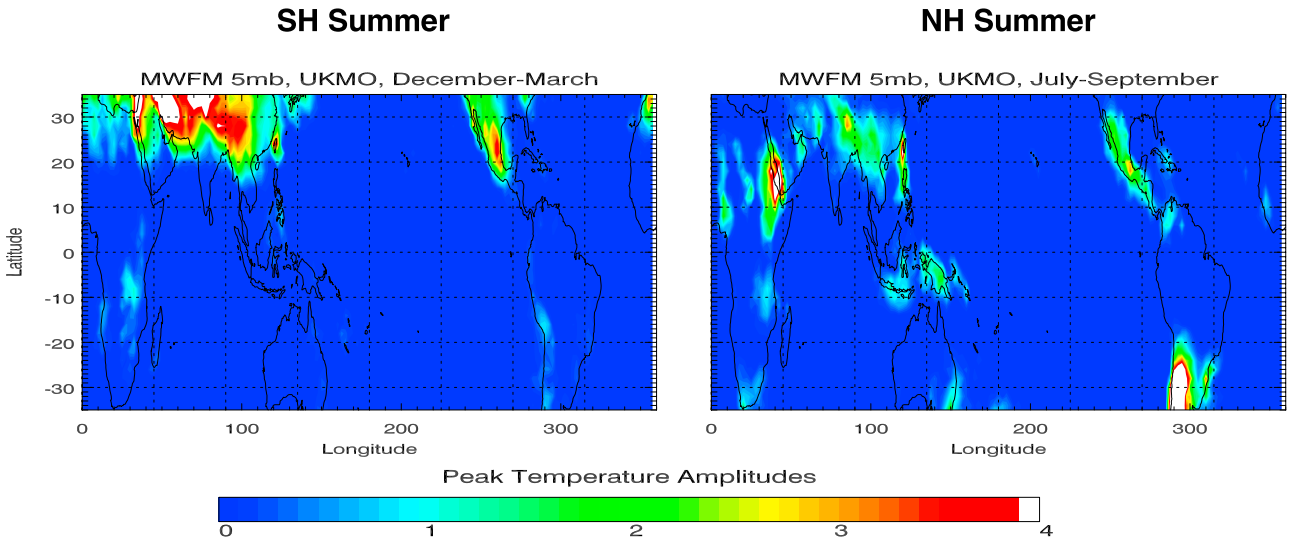

Figure 9. (left panel) NRL MWFM 2.1 simulated topography-related gravity waves for Southern Hemispheric summer (December–March 1991–1992). (right panel) Same but for Northern Hemisphere summer (July–September 1991–1992). Results are averaged over the same MLS measurement days.

meanwhile, westerlies occur in the Eastern Pacific and Atlantic Oceans (the "westerly duct"). The velocity potential and rainfall configurations are asymmetric about the equator. The SH subtropics is dominated by three major divergent centers over southeast Africa, Western Pacific, and South America. Deep convection related to the SH summertime monsoon is most pronounced across the Indonesian Seas and Western Pacific. The upper level divergent outflows from regions of heavy rains penetrate as far north as east China and Japan. This corresponds to the local Hadley circulation during the SH summer. The OLR and CMAP rainfall pattern indicate that convection mostly occurs across 10°N to 20°S latitudes. However, lowest OLR and highest rainfalls seem to concentrate on the Western Pacific and Indian oceans, southeast Africa, and South America. It is worth noting that the velocity potential and convective rainfall are both strongest over the Western Pacific, which is also the largest area of low OLR, high rainfall, and high cloudiness in the TTL (as shown in section 3).

[42] In July, when the NH summer is at its peak, the velocity potential, OLR, and rainfall fields exhibit asymmetry, with two major convective outflow centers about 10° to 15° north of the equator over South Asia and Central America, respectively. The July 150 hPa mean winds are also largely asymmetric about the equator. The NH is dominated by two prominent anticyclonic cells over Tibet and Mexico, with oceanic troughs over the Pacific and Atlantic oceans. The minimum OLR and maximum rainfall areas concentrate mostly over the Indian monsoon region and southeast Asia. Central America and northern Africa also have smaller centers of low OLR and heavy rainfalls. Note that there is a local maximum rainfall over the mouth of Red Sea which seems to be related to the GW pattern in Figure 4b.

[43] By combining the information from MLS measurements, MWFM, ECMWF winds, NOAA OLR, and CMAP results, geographic locations of deep-convection activity can be summarized as the follows (Figure 11): In NH winter/SH summer (December–March), continental deep convection usually occur in Central/Southern Africa and South America, while deep convection over water most frequently appears in the Western Pacific. The region over the maritime continent of Indonesia probably has combined land and oceanic convection. In NH summer/SH winter (June–September), major deep convection events occur in regions related to the Indian and Central America monsoons, plus some hurricanes (in the Gulf Mexico), typhoons (in southeast Asia), and other storm activities over the ocean.

5. Concluding Remarks and Future Work

[44] Geographical distributions of UTH, TTL cloudiness, and stratospheric GW variances have been analyzed from the UARS MLS observations. These MLS fields are compared with corresponding maps of ECMWF simulated wind divergence, as well as NOAA OLR and CMAP rainfall data for different seasons. The correlative pattern of these various parameter fields lead to an improved recognition of the causes and effects of tropical/subtropical convection in the tropopause and stratosphere worldwide. Combined evidence shows that most spatial and temporal variations of MLS measured GWs and cloudiness near the tropics are due to the occurrence of strong deep convection, which results in large spatial and seasonal variations in the air ascending into the TTL.

[45] In December–March, oceanic deep convection penetrates the bottom of tropopause significantly above the Western Pacific warm pool as indicated by the presence of high-altitude clouds near the top of TTL, by the strongest ECMWF velocity potential and wind divergence and by the lowest OLR and largest CMAP rainfall rates in the region. The deep convection overshoots of the tropical tropopause result in ~5% of ice clouds being lofted to altitude as high as ~68 hPa. A high rate of cloudiness in the TTL is also found over the convective regions of Africa and South America, but only a small fraction (≤1%) of the cloudiness

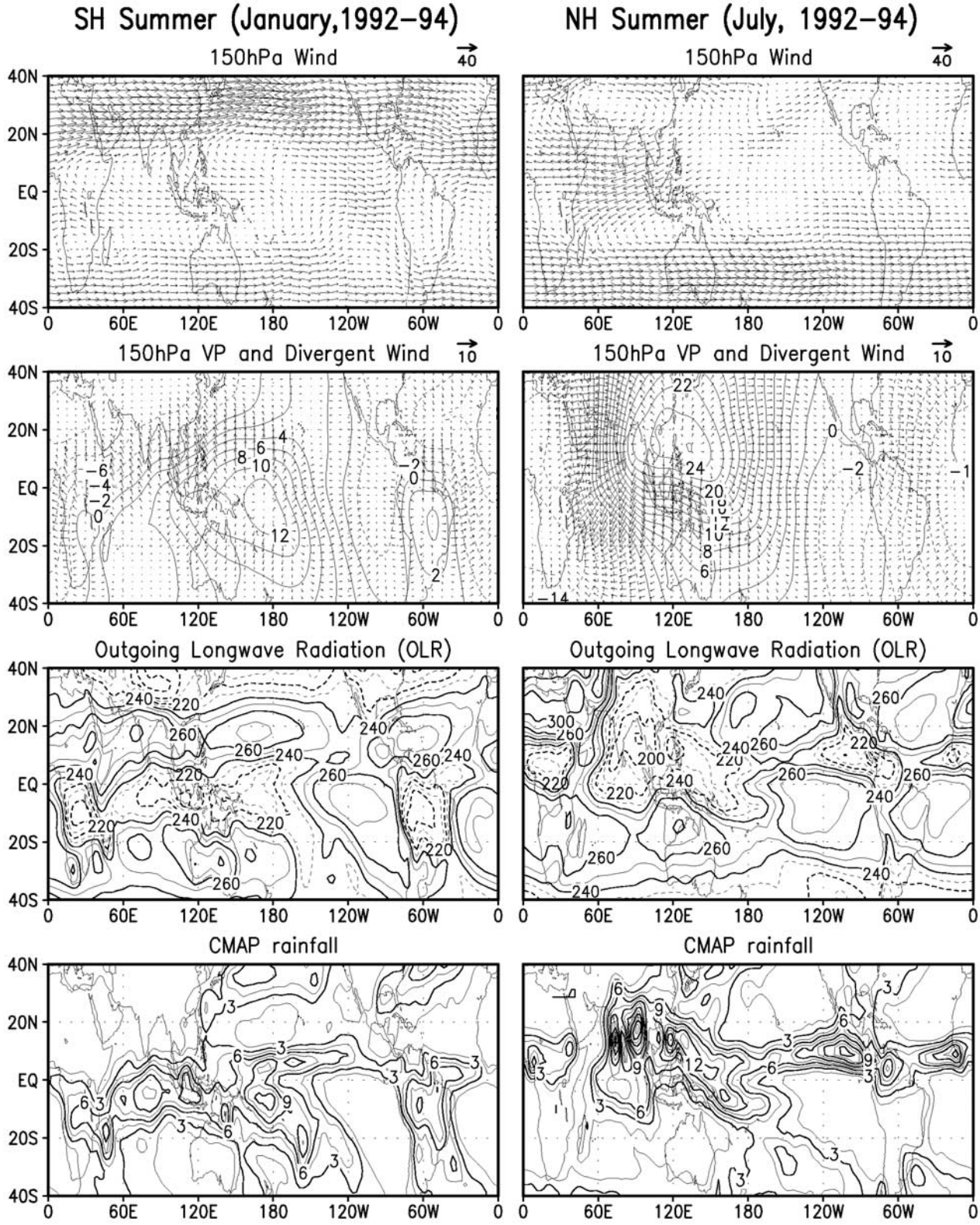

Figure 10. (left column) January 1992–1994 mean 150-mb winds (first row), velocity potential (interval 0.8×10^6 m^2 s^{-1}, dashed lines less than zero) and divergent winds (second row). The third row is January 1992–1994 mean OLR (contour unit is W/m^2; dashed lines less than 230 W/m^2). The bottom panel is CMAP January 1992–1994 mean rainfalls. (right column) As in left column except for July 1992–1994 means.

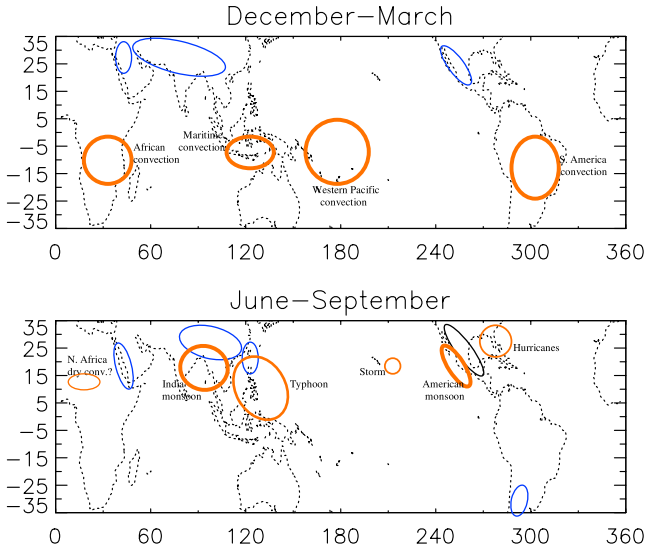

Figure 11. This simple diagram summarizes the approximate regions of major deep convection activities (red circles) and major topography related turbulences (blue circles), for SH (top panel) and NH (bottom panel) summers.

over these regions reaches altitudes above 100 hPa. The regions of lowest TTL temperatures (or "cold region") is seen to be correlated with the deep convection and located slightly downstream of the convection center. The region of minimum water vapor mixing ratio (or "dry region") near the top of TTL is also seen to be shifted slightly northwestward, downwind of the deep convection over the Western Pacific. This might imply that the rapid horizontal and vertical transport of air through cold regions dehydrates air as it ascends. Thus both vertical and horizontal motions are important for understanding the distribution of water vapor in the TTL.

[46] In July–September, the highest frequencies of cloudiness are found over the Indian to South Asia subcontinent and Central America. The extended Indian monsoon region corresponds to the strongest ECMWF velocity potential, lowest OLR, and largest CMAP rainfall rate in the area. Deep convection related to this Indian Monsoon lifts ~5% of ice clouds to altitude ~68 hPa. The moistening from the Indian and North American monsoons clearly results in two regions of high water vapor mixing ratio in the TTL up to ~100 hPa level, suggesting that continental monsoon convection may actually moisten the TTL rather than dehydrate it. The related TTL low-temperature regions above the Indian monsoon are somewhat southeastward of the convection area and also seem to following the wind pattern in the region. Minima in water vapor mixing ratios are not aligned well with the convection in this season, which may imply that dehydration in the TTL happens in regions away from convection.

[47] Strong stratospheric GWs radiated above the convective cloud tops are also measured by MLS. These GWs are well correlated with the major convection centers in both SH and NH summers and are seen shifted poleward by prevailing stratospheric winds, which agrees with background wind filtering theory.

[48] The time series of TTL cloudiness frequency for the three SH summertime regional deep convection show a slightly decreasing trend from 1991–1994. However, this may not be used as the evidence of a decline in convection events, since the time series of GW variances does not clearly show the same trend. Aside from the possible El Nino and Pinatubo effects, the interannual variations of water vapor and cloudiness might be an imprint of the interannual cycle of the minimum tropopause temperature on water vapor followed by slow ascent into the stratosphere as suggested by a recent model-measurement comparison study by *Read et al.* [2004].

[49] The above findings from the MLS measurements suggest that both the deep convection overshoot and the slow ascent mechanism are important to understand the complicated dehydration processes in the TTL. While making no judgment on these issues here, we would like to point out that deep convection disturbs an otherwise quiet TTL and thus affects the seasonal temperature and water vapor distributions there. Although the interannual variations in the TTL may indeed indicate a slow ascending trend according to *Read et al.* [2004], both "deep convection" and "slow ascent" mechanisms may play a role: deep convection is important on a shorter time scale (days to seasonal) and slow ascent on a longer time scale (interannual).

[50] Future observations and analyses of water vapor, ozone, temperature, clouds, and gravity waves data from the new generation EOS MLS and other instruments (e.g., HIRDLS and TES) on board the EOS Aura satellite (to be launched in 2004) will enable a complete convective pattern to be observed with global coverage and greatly improved space-time resolution to capture the dominant features of organized convection. The EOS MLS is specifically designed to measure water vapor with 0.1–0.2 ppmv precision throughout the TTL at 2.7 km vertical resolution. The cirrus ice measurement from EOS MLS may be able to show whether the ice masses in the TTL are lofted by deep convection. The EOS MLS upper tropospheric ozone measurements could also provide useful information. For example, low ozone levels near the TTL may indicate air that has been recently being transported from the boundary layer via deep convection. Thus a positive coincidence between regions of low water vapor and low ozone could support a convective dehydration hypothesis (A. E. Dessler, personal communication, 2003). These future endeavors will provide us with an integrated picture and better information of the dynamic and thermodynamic conditions in the TTL and the issues related to long-term stratospheric water vapor variations.

[51] **Acknowledgments.** Many initial ideas of this paper came from the discussions with the scientists attending the October 2002 Houston COSPAR conference. Joe W. Waters prepared the COSPAR presentation paper and fellow colleagues in the MLS science team provide encouragements and helpful suggestions. We thank J. R. Holton, J. C. McConnell, A. E. Dessler, and P. H. Haynes for helpful comments; M. J. Schwartz for carefully proofreading and suggested improvements; and G. Manney for UKMO wind and temperature data. This work was supported by the Jet Propulsion Laboratory, California Institute of Technology, under contract with the National Aeronautics and Space Administration. The authors also acknowledge the supports by Department of Meteorology, University of Hawaii; Geophysical Fluid Dynamics Laboratory at Kyushu University, Japan; the Naval Research Laboratory of Washington D.C.; and Computational Physics, Inc., Springfield, Virginia.

References

Alexander, M. J., J. R. Holton, and D. R. Durran (1995), The gravity wave response above deep convection in a squall line simulation, *J. Atmos. Sci.*, *52*, 2212–2226.

Alexander, M. J., J. H. Beres, and L. Pfister (2000), Tropical stratospheric gravity wave activity and relationship to clouds, *J. Geophys. Res.*, *105*, 22,299–22,309.

Boehm, M. T., and J. Verlinde (2000), Stratospheric influence on upper tropospheric tropical cirrus, *Geophys. Res. Lett.*, *27*, 3209–3212.

Brewer, A. M. (1949), Evidence for a world circulation provided by the measurements of helium and water vapor distribution in the stratosphere, *Q. J. R. Meteorol. Soc.*, *75*, 351–363.

Clark, H. L., A. Billingham, R. S. Harwood, and H. C. Pumphrey (2001), Water vapor in the tropical lower stratosphere during the driest phase of the atmospheric "tape recorder", *J. Geophys. Res.*, *106*, 22,695–22,705.

Dessler, A. E., and H. Kim (1999), Determination of the amount of water vapor entering the stratosphere based on Halogen Occulation Experiment (HALOE) data, *J. Geophys. Res.*, *104*, 30,605–30,607.

Dessler, A. E., and S. C. Sherwood (2000), Simulations of tropical upper tropospheric humidity, *J. Geophys. Res.*, *105*, 20,155–20,163.

Dewvan, E. M., R. H. Picard, R. R. O'Neil, H. A. Gardiner, J. Gibson, J. D. Mill, E. Richards, M. Kendra, and W. O. Gallery (1998), MSX satellite observations of thunderstorm-generated gravity waves in mid-wave infrared images of the upper stratosphere, *Geophys. Res. Lett.*, *25*, 939–942.

Fleming, E. L., S. Chandra, J. J. Barnett, and M. Corney (1990), Zonal mean temperature, pressure, zonal wind, and geopotential height as functions of latitude, *Adv. Space Res.*, *10*(12), 11–59.

Forster, P. M. D. F., and K. P. Shine (1999), Stratospheric water vapor changes as a possible contributor to observed stratospheric cooling, *Geophys. Res. Lett.*, *26*, 3309–3312.

Fovell, R., D. Durran, and J. R. Holton (1992), Numerical simulations of convectively generated stratospheric gravity waves, *J. Atmos. Sci.*, *49*, 1427–1442.

Fritts, D. C., and M. J. Alexander (2003), Gravity dynamics and effects in the middle atmosphere, *Rev. Geophys.*, *41*(1), 1003, doi:10.1029/2001RG000106.

Fritts, D. C., and T. E. VanZandt (1993), Spectral estimates of gravity wave energy and momentum fluxes, I, Energy dissipation, acceleration, and constraints, *J. Atmos. Sci.*, *50*, 3685–3694.

Gettelman, A., A. R. Douglass, and J. R. Holton (2000a), Simulations of water vapour in the upper troposphere and lower stratosphere, *J. Geophys. Res.*, *105*, 9003–9023.

Gettelman, A., et al. (2000b), Distribution and variability of water vapor in the upper troposphere and lower stratosphere, in *SPARC Assessment of Upper Tropospheric and Stratospheric Water Vapor*, *Rep. 2*, SPARC, Geneva.

Goya, K. (1998), Non-hydrostatic and compressible 2-D model simulations of internal gravity waves, doctoral thesis, Kyushu Univ., Kyushu, Japan.

Goya, K., and S. Miyahara (1998), A non-hydrostatic and compressible 2-D model simulation of Internal Gravity Waves generated by convection, *Earth Planet. Space*, *51*, 485–498.

Goya, K., and S. Miyahara (1999), Non-hydrostatic nonlinear 2-D model simulations of internal gravity waves in realistic zonal winds, *Adv. Space Res.*, *24*, 1523–1526.

Hall, T. J., and T. H. Vonder Harr (1999), The diurnal cycle of west Pacific deep convection and its relation to the spatial and temporal variations of tropical MCSs, *J. Atmos. Sci.*, *56*, 3401–3415.

Hendon, H. H., and K. Woodberry (1993), The diurnal cycle of tropical convection, *J. Geophys. Res.*, *98*, 16,623–16,637.

Highwood, E. J., and B. J. Hoskins (1998), The tropical tropopause, *Q. J. R. Meteorol. Soc.*, *124*, 1579–1604.

Holton, J. R. (1992), *An Introduction to Dynamic Meteorology*, 3rd ed., Academic, San Diego, Calif.

Holton, J. R., and A. Gettelman (2001), Horizontal transport and the dehydration of the stratosphere, *Geophys. Res. Lett.*, *28*, 2799–2802.

Holton, J. R., M. J. Alexander, and M. T. Boehm (2001), Evidence for short vertical wavelength Kelvin waves in the DOE-ARM Nauru99 radiosonde data, *J. Geophys. Res.*, *106*, 20,125–20,129.

Horel, J. D., A. N. Hahmann, and J. E. Geisler (1989), An investigation of the annual cycle of convective activity over the tropical Americas, *J. Clim.*, *2*, 1388–1403.

Huffman, G. J., R. F. Adler, P. Arkin, A. Chang, R. Ferraro, A. Gruber, J. Janowiak, A. McNab, B. Rudolf, and U. Schneider (1997), The Global Precipitation Climatology Project (GPCP) combined precipitation dataset, *Bull. Am. Meteorol. Soc.*, *78*, 5–20.

Jensen, E. J., O. B. Toon, H. B. Selkirk, J. D. Spinhime, and M. R. Schoberl (1996), On the formation and persistence of subvisible cirrus clouds near the tropical tropopause, *J. Geophys. Res.*, *101*, 21,361–21,375.

Jiang, J. H., and D. L. Wu (2001), UARS MLS observation of gravity waves associated with the Arctic winter stratospheric vortex, *Geophys. Res. Lett.*, *28*, 527–530.

Jiang, J. H., D. L. Wu, and S. D. Eckermann (2002), Upper Atmosphere Research Satellite (UARS) MLS observation of mountain waves over the Andes, *J. Geophys. Res.*, *107*(D22), 8273, doi:10.1029/2002JD002091.

Jiang, J. H., S. D. Eckermann, D. L. Wu, and J. Ma (2003), Mountain waves in the middle atmosphere: Microwave Limb Sounder observations and analyses, *Adv. Space Res.*, *32*, 801–806.

Jiang, J. H., S. D. Eckermann, D. L. Wu, and J. Ma (2004), A search for mountain waves in MLS stratospheric limb radiances from the winter northern hemisphere: Data analysis and global mountain wave modeling, *J. Geophys. Res.*, *109*, doi:10.1029/2003JD003974.

Johnson, R. H., and D. C. Kriete (1982), Thermodynamic and circulation characteristics of winter monsoon tropical mesoscale convection, *Mon. Weather Rev.*, *110*, 1898–1911.

Johnston, H. S., and S. Solomon (1979), Thunderstorms as possible micrometeorological sink for stratospheric water, *J. Geophys. Res.*, *84*, 3155–3158.

Karoly, D. J., G. L. Roff, and M. J. Reeder (1996), Gravity wave activity associated with tropical convection detected in TOGA COARE sounding data, *Geophys. Res. Lett.*, *23*, 261–264.

Kim, Y. J., S. D. Eckermann, and H.-Y. Chun (2003), An overview of the past, present and future of gravity-wave drag parametrization for numerical climate and weather prediction models, *Atmos. Ocean*, *41*, 65–98.

Kirk-Davidoff, D. B., E. J. Hintsa, J. G. Anderson, and D. W. Keith (1999), The effect of climate change on ozone depletion through changes in stratospheric water vapour, *Nature*, *402*, 399–401.

Koch, S. E., and L. M. Siedlarz (1999), Mesoscale gravity waves and their environment in the central United States during STORM-FEST, *Mon. Weather Rev.*, *127*, 2854–2879.

Lane, T. P., M. J. Reeder, and T. L. Clark (2001), Numerical modeling of gravity wave generation by deep tropical convection, *J. Atmos. Sci.*, *58*, 1249–1274.

Liu, G., J. A. Curry, and R. S. Sheu (1995), Classification of clouds over the western equatorial Pacific Ocean using combined infrared and microwave satellite data, *J. Geophys. Res.*, *100*, 13,811–13,826.

Liu, X., and J. Penner (2002), Effect of Mount Pinatubo H_2SO_4/H_2O aerosol on ice nucleation in the upper troposphere using a global chemistry and transport model, *J. Geophys. Res.*, *107*(D12), 4141, doi:10.1029/2001JD000455.

Livesey, N. J., and D. L. Wu (1999), Eos MLS retrieval processes algorithm theoretical basis, *JPL Doc, D-16159*, Jet Prop. Lab., Pasadena, Calif.

Livesey, N. J., W. G. Read, L. Froidevaux, J. W. Waters, H. C. Pumphrey, D. L. Wu, M. L. Santee, Z. Shippony, and R. F. Jarnot (2003), The UARS Microwave Limb Sounder version 5 dataset: Theory, characterization and validation, *J. Geophys. Res.*, *108*(D13), 4378, doi:10.1029/2002JD002273.

Lohmann, U., B. Kaercher, and C. Timmreck (2003), Impact of the Mt. Pinatubo Eruption on cirrus clouds formed by homogeneous freezing in the ECHAM GCM, *J. Geophys. Res.*, *108*(D18), doi:10.1029/2002JD003185.

Mapes, B., and R. Houze (1993), Cloud clusters and superclusters over the oceanic warm pool, *Mon. Weather Res.*, *121*, 1398–1415.

Massie, S., P. Lowe, X. Tie, M. Hervig, G. Thomas, and J. Russell III (2000), Effect of the 1997 El Nino on the distribution of upper tropospheric cirrus, *J. Geophys. Res.*, *105*, 22,725–22,741.

McLandress, C., M. J. Alexander, and D. L. Wu (2000), Microwave Limb Sounder observations of gravity waves in the stratosphere: A climatology and interpretation, *J. Geophys. Res.*, *105*, 11,947–11,967.

Mitchell, T. P., and J. M. Wallace (1992), Annual cycle in equatorial convection and sea-surface temperature, *J. Clim.*, *5*, 1140–1156.

Mote, P. W., K. H. Rosenlof, M. E. McIntyre, E. S. Carr, J. R. Holton, J. S. Kinnersley, H. C. Pumphrey, J. M. Russell III, J. W. Waters, and J. C. Gille (1996), An atmospheric tape recorder: The imprint of tropical tropopause temperatures on stratospheric water vapor, *J. Geophys. Res.*, *101*, 3989–4006.

Motell, C. E., and B. C. Weare (1987), Estimating tropical Pacific rainfall using digital satellite data, *J. Clim. Appl. Meteorol.*, *26*, 1436–1446.

Murakami, T., and B. Wang (1993), Annual cycle of Equatorial east-west circulation over the India Pacific oceans, *J. Clim.*, *6*, 932–952.

Newell, R. E., and S. Gould-Stewart (1981), A stratospheric fountain?, *J. Atmos. Sci.*, *38*, 2789–2796.

Preusse, P., G. Eidmann, S. D. Eckermann, B. Schaeler, R. Spang, and D. Offermann (2001), Indications of convectively generated gravity waves in CRISTA temperatures, *Adv. Space. Res.*, *27*(10), 1653–1658.

Randel, W. J., and F. Wu (2003), Thermal variability of the tropical tropopause region derived from GPS/MET observations, *J. Geophys. Res.*, *108*(D1), 4024, doi:10.1029/2002JD002595.

Randel, W. J., F. Wu, and D. Gaffen (2000), Low frequency variations of the tropical tropopause from NCEP reanalyses, *J. Geophys. Res.*, *105*, 15,509–15,523.

Randel, W. J., F. Wu, A. Gettelman, J. M. R. III, J. M. Zawodny, and S. J. Oltmans (2001), Seasonal variation of water vapor in the lower stratosphere observed in Halogen Occultation Experiment data, *J. Geophys. Res.*, *106*, 14,313–14,325.

Read, W. G., et al. (2001), UARS microwave limb sounder upper tropospheric humidity measurement: Method and validation, *J. Geophys. Res.*, *106*, 32,207–32,258.

Read, W. G., et al. (2004), Dehydration in tropical tropopause layer: Implications from UARS MLS, *J. Geophys. Res.*, *109*, doi:10.1029/2003JD004056, in press.

Roach, R., and V. Ramanathan (2000), Scale dependence of monsoonal convective systems over the Indian ocean, *Clim, J.*, *13*, 1286–1298.

Salby, M. L. (1996), *Fundamentals of Atmospheric Physics*, 440 pp., Academic, San Diego, Calif.

Sato, K., H. Hashiguchi, and S. Fukao (1995), Gravity waves and turbulence associated with cumulus convection observed with the UHF/VHF clear-air Doppler radars, *J. Geophys. Res.*, *100*, 7111–7120.

Sherwood, S. C. (2000), A ''stratospheric drain'' over the martitime continent, *Geophys. Res. Lett.*, *27*, 677–680.

Sherwood, S. C., and A. E. Dessler (2000), On the control of stratospheric humidity, *Geophys. Res. Lett.*, *27*, 2513–2516.

Sherwood, S. C., and A. E. Dessler (2001), A model for transport across the tropical tropopause, *J. Atmos. Sci.*, *58*, 765–779.

Soden, B. (2000), The diurnal cycle of convection, clouds, and water vapor in the tropical upper troposphere, *Geophys. Res. Lett.*, *27*, 2173–2176.

Teitelbaum, H., M. Moustaoui, C. Basdevant, and J. R. Holton (2000), An alternative mechanism explaining the hygropause formation in tropical region, *Geophys. Res. Lett.*, *27*, 221–224.

Tsuda, T., Y. Murayama, H. Wiryosumarto, S. W. B. Harijino, and S. Kato (1994a), Radiosonde observations of equatorial atmospheric dynamics over Indonesia: 1. Equatorial waves and diurnal tides, *J. Geophys. Res.*, *99*, 10,491–10,505.

Tsuda, T., Y. Murayama, H. Wiryosumarto, S. W. B. Harijino, and S. Kato (1994b), Radiosonde observations of equatorial atmospheric dynamics over Indonesia: 2. Characteristics of gravity waves, *J. Geophys. Res.*, *99*, 10,507–10,516.

Tsuda, T., M. Nishida, C. Rocken, and R. H. Ware (2000), A global morphology of gravity wave activity in the stratosphere revealed by the GPS occultation data (GPS/MET), *J. Geophys. Res.*, *105*, 7257–7273.

Vadas, S. L., D. C. Fritts, and M. J. Alexander (2003), Mechanism for the generation of secondary waves in wave breaking regions, *J. Atmos. Sci.*, *60*, 194–214.

Wang, B. (1994a), On the annual cycle in the tropical eastern central Pacific, *J. Clim.*, *7*, 1926–1942.

Wang, B. (1994b), Climate regimes of tropical convection and rainfall, *J. Clim.*, *7*, 1109–1118.

Waters, J. W., et al. (1999), The UARS and EOS microwave limb sounder experiments, *J. Atmos. Sci.*, *56*, 194–218.

Wu, D. L., and J. H. Jiang (2002a), MLS observation of atmospheric gravity waves over Antarctica, *J. Geophys. Res.*, *107*(D24), 4773, doi:10.1029/2002JD002390.

Wu, D. L., and J. H. Jiang (2002b), EOS MLS algorithm theoretical basis for cloud measurements, *Tech. Rep. D-19299*, Jet Prop. Lab., Pasadena, Calif.

Wu, D. L., and J. W. Waters (1996a), Satellite observations of atmospheric variances: A possible indication of gravity waves, *Geophys. Res. Lett.*, *23*, 3631–3634.

Wu, D. L., and J. W. Waters (1996b), Gravity-wave-scale temperature fluctuations seen by the UARS MLS, *Geophys. Res. Lett.*, *23*, 3289–3292.

Xie, P., and P. A. Arkin (1997), Global precipitation: A 17-year monthly analysis based on gauge observations, satellite estimates, and numerical model outputs, *Bull. Am. Meteorol. Soc.*, *78*, 2539–2558.

Zhou, X., M. A. Geller, and M. Zhang (2001), The cooling trend of the tropical cold point tropopause temperatures and its implications, *J. Geophys. Res.*, *106*, 1511–1521.

S. D. Eckermann, Middle Atmosphere Dynamics Section, Naval Research Laboratory, 4555 Overlook Avenue SW, Washington, DC 20375, USA. (eckerman@uap2.nrl.navy.mil)

K. Hocke, Max-Planck-Institut fur Aeronomie, Max-Planck-Str. 2, 37191 Katlenburg-Lindau, Germany. (sigrid.hocke@t-online.de)

K. Goya, Geophysical Fluid Dynamics Laboratory, Kyushu University, Hakozaki, Fukuoka, 812-8581, Japan. (goya@geo.kyushu-u.ac.jp)

J. H. Jiang, W. G. Read, and D. L. Wu, Jet Propulsion Laboratory, California Institute of Technology, Mail Stop 183-701, 4800 Oak Grove Drive, Pasadena, CA 91109-8099, USA. (jonathan@mls.jpl.nasa.gov; bill@mls.jpl.nasa.gov; dwu@mls.jpl.nasa.gov)

J. Ma, Computational Physics Inc., 8001 Braddock Road, Springfield, VA 2215, USA. (junma@uap2.nrl.navy.mil)

B. Wang, Department of Meteorology, University of Hawaii, 1680 East West Road, Honolulu, HI 96822, USA. (wangbin@hawaii.edu)